Research Square

Preprints are preliminary reports that have not undergone peer review.
They should not be considered conclusive, used to inform clinical practice,
or referenced by the media as validated information.

New Description of the Fine scale dynamics around Fernando de Noronha and Rocas Atoll provided by SWOT

Diógenes Passos Fontenele

diogenesfontenele13@gmail.com

Universidade Federal do Ceará

Fabrice Hernandez

Laboratoire d'Études en Géophysique et Océanographie Spatiales

Antonio Geraldo Ferreira

Universidade Federal do Ceará

Eduardo Sávio P. R. Martins

Fundação Cearense de Meteorologia e Recursos Hídricos

Research Article

Keywords: Tropical Atlantic Ocean, Satellite Altimetry, Island Effect, Submesoscale Dynamics

Posted Date: April 21st, 2026

DOI: https://doi.org/10.21203/rs.3.rs-9334419/v1

License: This work is licensed under a Creative Commons Attribution 4.0 International License.
Read Full License

Additional Declarations: No competing interests reported.

Abstract

Using SWOT and conventional nadir altimetric data, we investigate the surface signature of the Island Mass Effect (IME) around the Fernando de Noronha Archipelago and the Rocas Atoll in the western tropical Atlantic. Across the islands, the central branch of the South Equatorial Current (cSEC) flows westward at the surface while the eastward South Equatorial Undercurrent (SEUC) flows below in the thermocline, generating complex dynamics such as eddies, wakes, and upwelling that enhance local productivity in otherwise oligotrophic waters. Over the 2023–2024 period, we explore whether submesoscale surface features associated with IME can be detected, using in addition SST and ocean color products. Using eddy tracking techniques, the SWOT data reveal numerous cyclonic and anticyclonic eddies with radii typically below 15 km, often co-located with cold sea surface temperature anomalies and elevated chlorophyll-a concentrations. These patterns indicate submesoscale-driven upwelling processes that promote nutrient supply and biological productivity, providing direct observational evidence of IME at the surface. The spatial variability of vertical exchanges, inferred from SST Laplacian analysis, highlights the complexity of these processes. A comparison with conventional altimetry products (DUACS/MIOST) and the GLORYS12V1 global ocean reanalysis shows that these datasets fail to resolve such fine-scale structures due to their coarser resolution and smoothing effects. In contrast, SWOT significantly improves detection capability, capturing eddies as small as 3 km and low-amplitude signals. Overall, this study demonstrates that SWOT enables the observation of previously unresolved submesoscale dynamics around small oceanic islands, offering new insights into the coupling between physical processes and marine ecosystems, and advancing the understanding of ocean circulation in insular environments.

1. Introduction

The Fernando de Noronha Archipelago and Rocas Atoll, located in the western tropical Atlantic (respectively at 3°51’S–32°25’W and 3°52’S–33°49’W), are characterized by fine-scale ecological and oceanographic processes associated with their topographic setting and the influence of major current systems. Recent studies have highlighted the role of the archipelago and atoll in modulating regional circulation, creating favorable conditions for enhanced biodiversity and productivity, despite being surrounded by oligotrophic waters (Tchamabi et al. 2017; Costa da Silva et al. 2021; Lira et al. 2024).

As shown by the Mean Dynamic Topography (MDT, Fig. 1), the Fernando de Noronha Archipelago and the Rocas Atoll are surrounded at the surface by the general northwest-westward flow of the South Equatorial Current (SEC). They are influenced by the western boundary system along the Brazilian shelf, formed by the surface North Brazil Current (NBC), with underneath the North Brazil UnderCurrent (NBUC). These currents feed eastward recirculation at depth, with the South Equatorial Undercurrent (SEUC) that drives thermocline waters around the islands (Dossa et al. 2022).

In this context, the interaction between the central branch of the SEC (cSEC) and the SEUC, with the island topography has been identified as a key mechanism driving the formation of eddies, wake effects,

and upwelling zones. These processes influence nutrient dynamics and primary productivity in the region, favoring the occurrence of plankton blooms and the development of pelagic and benthic communities around the islands with the so-called “Larval Island Effect” (Lira et al. 2014; Lira et al. 2024).

These processes are referred to as the *Island Mass Effect* (IME) and were first described in the 1950s by Doty and Oguri (1956). By definition, IME refers to the set of physical and biological processes occurring downstream of islands and reefs (Hammer and Houri, 1981). Several studies have sought to describe how islands perturb oceanic flows. In some cases, local atmospheric perturbations drive the oceanic responses around the island (e.g., Alves et al. 2021). But the direct role of the oceanic dynamics in interactions with the island should also be considered. Processes such as island wakes (Barton, 2001), upwelling and vertical mixing (Hasegawa 2009), and the generation of cyclonic vortices resulting from barotropic or baroclinic instabilities downstream of islands known as von Kármán vortex streets (Teinturier et al. 2010) are among the proposed physical mechanisms.

Like in the overall West Tropical Atlantic, the surface layer temperature exhibits a seasonal cycle with the maximum exceeding 28°C from March to April and minimum around 26°C from August to October (e.g., Tchamabi et al. 2017).

Associated with this mean flow, the IME has been observed through peaks in chlorophyll-a fluorescence, shoaling of the thermocline downstream of the islands, and subsurface cooling promoted by the interaction between the cSEC and the island bathymetry. Subsurface vortices near the archipelago have also been detected in response to the IME in the downstream region of the islands (Costa da Silva et al. 2021; Lira et al. 2024).

Despite the subsurface signature of the IME in this region, it remains unclear whether and how these processes manifest at the ocean surface, particularly at spatial scales comparable to the island size. Understanding whether such surface expressions exist is essential to clarify the role of island-induced dynamics in mediating energy transfer and circulation at small spatial scales.

According to Dong et al. (2007), when the Reynolds number is sufficiently high (above 50–60), the island wake becomes unstable and vortices detach from its flanks, forming a von Kármán vortex street. The size of these vortices is on the order of the island scale, which is a likely reason why current observations have not yet detected surface physical processes around the island.

With the advancement of the Surface Water and Ocean Topography (SWOT) mission (Fu et al. 2024), a new observational capability is now available to describe ocean circulation at finer scales, providing an opportunity to investigate surface processes at the submesoscale. Data acquired by the onboard sensors enable the mapping of sea surface height (SSH) at spatial resolutions ranging from 5 to 15 km. This advancement allows for the detection and analysis of submesoscale features such as vortices, fronts, and filaments, which play an important role in ocean mixing and biogeochemical processes (Archer et al. 2025, Carli et al. 2025).

Recent SWOT results have revealed new insights into small-scale ocean variability, including vortices with radii on the order of 10–25 km, internal waves, and oceanic fronts in different regions such as the Kuroshio Current, the Southern Ocean, the Mediterranean Sea, and the South China Sea (Qiu and Chen 2025; Verger-Miralles et al. 2025; Zhang et al. 2025). These observations are already reshaping the understanding of the coupling between physical and oceanic processes (Tzortzis et al. 2021) and highlight the potential of SWOT to resolve fine-scale dynamics in regions where conventional altimetry has been limited. Given these improvements in spatial resolution, it remains necessary to assess whether such observational capabilities are sufficient to resolve the surface expression of island-induced dynamics, which have so far been inferred mainly from subsurface observations. As a first approximation, it could be assumed that SWOT may capture the surface signatures comparable to the island size, which have remained unresolved by previous observing systems.

In this sense, this study aims to examine whether island-induced dynamics associated with the Island Mass Effect exhibit a detectable surface signature at submesoscale spatial scales around small oceanic islands. To address this question, the capability of SWOT-derived products to characterize submesoscale variability around the Fernando de Noronha Archipelago and the Rocas Atoll is examined, emphasizing the improvement provided by SWOT relative to conventional altimetric datasets.

This approach provides new insight into the surface expression of island-induced dynamics and clarifies the extent to which recent altimetric advances enhance the representation of fine-scale circulation in insular environments. Consequently, this will make possible to assess the value of SWOT data for describing the mesoscale and submesoscale, in combination with other recent, higher-resolution datasets, such as sea surface temperature from MUR and chlorophyll-*a* from Sentinel-3A/3B (OLCI) and Copernicus-GlobColour (SeaWiFS, MODIS Aqua, MODIS Terra, MERIS, VIIRS-SNPP, VIIRS-JPSS1, OLCI-S3A and S3B). The progress made by SWOT will be measured by comparison with coarser-resolution products, including the largely used sea level estimates satellite altimetry gridded product DUACS/MIOST and the global ocean reanalysis GLORYS12V1.

This article first describes the data used in section 2, and then details the expected ocean dynamics around the islands in section 3. Section 4 informs on the methodology, and Section 5 presents and discusses the results. Finally, Section 6 summarizes the main findings and conclusions.

2. Data Used

2.1 Satellite Data

Prior to the SWOT era, oceanic islands and coastal regions were observed using nadir-looking satellite altimetry missions since 1991 with similar orbit series: TOPEX/Jason1/2/3 and recently Sentinel-6A ; ERS1/2, Envisat, and SARAL/AltiKa ; Geosat Follow-on (GFO), CryoSat-2 ; HY-2A/B, and Sentinel3A/B. The 1 Hz XTRACK dataset (Birol et al., 2017) that provides historical nadir altimeter along-track mission reprocessed, gives an overview of the sea level variability in the region of interest over three decades.

As illustrated by Fig. 2 along the latitudinal band of the archipelago, conventional altimetry provides one-dimensional (1-D) ground tracks with limited cross-track sampling and reduced resolution near the coast and in regions of complex bathymetry, thereby hindering the monitoring of insular environments (Vignudelli et al. 2019; Liu et al. 2023). In addition to their limited spatial resolution, altimetric measurements in nearshore regions are affected by radar echo contamination and increased noise within a band of up to 10 km from the coast or islands (Vignudelli et al. 2019; Shi et al. 2025). Consequently, with conventional nadir altimeters, the effective resolution in these regions is on the order of 100–200 km.

The along-track sea level variability in the area is of the order of 3–8 cm rms (Fig. 2), typical of tropical large scale dynamics. Differences between neighboring tracks are visible: due to the temporal length of available along track repeated time series, as well as intrinsic quality of each satellite mission. The recent satellite datasets from the Sentinel program offer less along-track noise. Advances in radar technology, including fully focused SAR (FFSAR) processing and the use of Ka-band altimetry, have led to improvements in altimetric data retrieval through waveform decontamination and enhanced retracking techniques (La Vu et al. 2018; Morrow et al. 2018; Peng et al. 2023; Shi et al. 2025). These developments have improved the quality of sea surface height anomaly (SSHA) data; however, the effective resolution and accuracy have remained insufficient to resolve submesoscale and small-scale features in many insular environments (Morrow et al. 2018; Liu et al. 2023).

In this context, ocean mapping based on conventional altimeter data also represented an important advance in the representation of oceanic features in insular environments. Since the early 2000s, the DUACS (Data Unification and Altimeter Combination System) framework has produced Level-4 (L4) multi-mission products of sea level anomaly (SLA) and absolute dynamic topography (ADT), providing high-quality altimetric information widely used in studies of ocean dynamics, climate, and operational oceanography (Le Traon et al., 2025). According to these authors, the quality and relevance of DUACS products result from several factors, including the number of altimeters considered over time, retracking procedures, the application of multiple environmental and geophysical corrections, and the mapping methods employed.

The evolution of DUACS products from DT2014, DT2018, and DT2021 to the current DT2024 version reflects a series of progressive improvements in altimetric standards and geophysical corrections, with particular emphasis on tidal treatment, as well as refinements of optimal interpolation parameters tailored for global and regional products and for regions of high variability (Ballarotta et al. 2019; Taburet et al. 2019). The DT-2024 version used in this study introduces a new mapping method in the Level-4 products, referred to as the Multiscale Inversion of Ocean Surface Topography (MIOST), which replaces single-scale optimal interpolation covariances with multiscale covariances associated with distinct surface dynamic processes. The daily product with a 0.125° x 0.125° resolution from 1993 to 2025 is downloaded from the Copernicus Marine Data Store (CMDS).

This latest release also incorporates SWOT v2.0.1 observations into the multi-mission framework (Ubelmann et al. 2021; Ballarotta et al. 2024). As a result, a global mean effective SLA resolution of approximately 180 km is achieved at mid-latitudes, becoming finer toward the poles (Le Traon et al. 2025). For comparison, the previous version generated using conventional optimal interpolation, without SWOT data, was also evaluated. However, as illustrated by the Fig. 2, the sea level variability from the DUACS/MIOST daily product around the archipelago exhibits a smooth, large scale pattern that does not reflect neither the shorter space scales of this variability captured along-track by the XTRACK product, nor the higher variability expected with the island-induced dynamics.

Since the science phase of SWOT started after July 2023, two-dimensional SSH data with an approximate resolution of 2 km are providing around the island a significant improvement in spatial resolution compared to conventional nadir altimeter tracks. In insular regions, SWOT measurements reduce root mean square (RMS) errors by approximately 40–60% relative to nadir observations. In addition, SWOT derived geoid estimates recover fine-scale signals and remove bubble-like noise in the mean dynamic topography (MDT) near islands (Wu et al. 2025; Yu et al. 2025). These capabilities are expected to enable more accurate measurements of fine-scale variability and improved SSHA mapping in complex environments such as oceanic islands.

In this study, only data from the SWOT science phase are used, because the calibration and validation (Cal/Val) phase orbit (March-July 2023) did not provide satellite measurements around the archipelago. These data are acquired by the Ka-band synthetic aperture radar interferometer (KaRIn), operating in nominal wide-swath mapping mode. The sensor provides two-dimensional fields of sea surface height (SSH) and related variables along a fixed-geometry swath, with its performance evaluated globally during the Cal/Val phase (Morrow et al. 2019). The antenna consists of two swaths, each approximately 50 km wide, separated by a gap of about 20 km for which only nadir satellite data are available (Morrow et al., 2023). This configuration yields a total cross-track coverage of 120 km and an orbital repeat cycle of 21 days. With an inclination of 78°, the sensor enables imaging between 78°N and 78°S, covering nearly all of the global oceans (Chelton 2024).

From the AVISO+ repository, the SWOT KaRIn Level-3 Expert product, version 3.0, filtered dataset is used here, with an approximate spatial resolution of 2 km × 2 km, capable of resolving spatial scales on the order of 15 km at low latitudes (Wang et al. 2019). According to Wang et al. (2025), geostrophic variables and SSH are resolved at scales ranging from 20 to 100 km with errors two to four times smaller than those expected prior to the satellite launch. A detailed description of the SWOT KaRIn Level-3 expert product is provided in Dibarboure et al. (2025), which involves processing Level-2 data from its original 250 m x 250 m resolution into the 2 km x 2 km expert dataset.

2.2 Sea Surface Temperature

Sea surface temperature (SST) fields were analyzed over the western tropical Atlantic, encompassing the Fernando de Noronha Archipelago and the Rocas Atoll, to identify SST anomalies potentially associated with upwelling events linked to submesoscale dynamics near the islands. The Version 4

Multiscale Ultrahigh Resolution (MUR) product was used, derived from nighttime GHRSST L2P skin and subskin SST observations acquired by multiple sensors, including the NASA Advanced Microwave Scanning Radiometer-EOS (AMSR-E), the JAXA Advanced Microwave Scanning Radiometer 2 onboard GCOM-W1, the Moderate Resolution Imaging Spectroradiometers (MODIS) aboard the NASA Aqua and Terra platforms, the US Navy WindSat microwave radiometer, the Advanced Very High Resolution Radiometer (AVHRR) on several NOAA satellites, and in situ SST observations from the NOAA iQuam project (Chin et al. 2017; Koutantou et al. 2023).

These datasets are merged using the Multi-Resolution Variational Analysis (MRVA) algorithm to produce a global daily analysis on a 0.01° x 0.01° grid (Chin et al. 2017). Data was collected from the NASA PODAAC repository. The period 2003–2023 was used to compute a daily climatology, from which daily anomalies were derived for August 2023 to August 2024. These anomalies were subsequently examined in conjunction with the identified eddies in order to assess their association with upwelling-related dynamics.

2.3 Chlorophyll-a

Primary productivity around the islands was inferred from phytoplankton chlorophyll-*a* concentrations (Davies et al. 2018) derived from two products. The Level-4 (L4) Copernicus-GlobColour product, a global multi-sensor and cloud-free dataset, was used as the primary reference. This product collected from the CMDS has a spatial resolution of 4 km and is provided at daily temporal resolution.

In addition, Level-3 (L3) data from the Ocean and Land Colour Instrument (OLCI) onboard the Sentinel-3A (S3A) and Sentinel-3B (S3B) satellites were analyzed at a spatial resolution of 300 m. Although affected by cloud coverage, the higher-resolution OLCI observations were useful to confirm days of elevated primary productivity identified in the L4 product. The products are produced by ACRI-ST (Sophia Antipolis, France) and distributed through the CMDS (Xi et al. 2020).

2.4 GLORYS12V1 Reanalysis

GLORYS is a global ocean reanalysis project in which a horizontal resolution of 1/12° simulation covering from 1993 to the present has been initiated (Lellouche et al. 2021). The version 1 (GLORYS12V1, also called hereafter G12V1) is produced in operation within the Copernicus Marine Service and is generated using the NEMO/ORCA12 model (50 z-levels), which is forced by the ECMWF ERA-Interim atmospheric reanalysis and, in more recent years, by ERA5 (Lellouche et al. 2021). Daily and monthly-mean datasets have been downloaded from the CMDS.

During product generation, the assimilation system incorporates altimetric SLA data, SST, and temperature–salinity profiles using a Kalman filter combined with a three-dimensional variational (3D-Var) bias correction scheme, ensuring dynamical consistency between SSH fields and ocean currents (Lellouche et al. 2021; Verezemskaya et al. 2021). Because SLA is directly assimilated, both the SSH field and its variability are generally well reproduced at meso- and large scales, capturing expected patterns of global circulation (Lellouche et al. 2021). In regions with highly energetic boundary currents, such as

the Agulhas, Gulf Stream, the Kuroshio or the California Currents, G12V1 accurately represents fronts and meanders observed in satellite data, with SSH contours providing a proxy for the structure and variability of surface geostrophic jets (e.g. Russo et al. 2022; Amaya et al. 2023a).

It is also worth noting that, owing to its 1/12° horizontal grid, G12V1 resolves mesoscale eddies and associated surface velocity variability more effectively than equivalent products with a 1/4° resolution (Jean-Michel et al. 2021; Verezemskaya et al. 2021). Amaya et al., (2023b) also show that deep heat anomalies along the north american continental shelves are well represented by G12V1. Nevertheless, despite its widespread use, G12V1 may exhibit limitations in the western tropical Atlantic. According to Dossa et al. (2021), the reanalysis incorrectly positions the core of the North Brazil Undercurrent (NBUC), with an offshore displacement of approximately 15 km relative to observations, and presents an inversion of the seasonal cycle of water mass transport. For these reasons, G12V1 data are carefully evaluated around Fernando de Noronha archipelago and Rocas Atoll in this study.

3. General circulation around the Fernando de Noronha Archipelago and the Rocas Atoll

The Fernando de Noronha Archipelago, located approximately 350 km off the northeastern Brazilian coast in the western South Atlantic, consists of a group of 21 volcanic islands. Its main island, which gives its name to the archipelago, is inhabited and has an approximate length of 11 km and a width of 3 km (Moreira et al. 2018).

The region is characterized by a tropical oceanic climate, with a mean annual temperature of approximately 25–27°C and an annual precipitation of about 1400 mm, marked by distinct dry (March–June) and wet (August–January) seasons (Mohr et al. 2009; Barcellos et al. 2017). Rainfall variability in the region is primarily controlled by the Intertropical Convergence Zone (ITCZ), which also regulates the trade winds and influences thermocline variability and near-surface circulation (Servain et al. 2014; Hounsou-Gbo et al. 2019; Assunção et al. 2020; Costa da Silva et al. 2021).

As illustrated by Fig. 1, ocean circulation around the archipelago is dominated by the central branch of the South Equatorial Current (cSEC), which flows from east to west within the upper 100 m of the water column. Below this layer, the circulation reverses direction, with waters flowing from west to east through the South Equatorial Undercurrent (SEUC), predominantly located between 3°S and 5°S (Assunção et al. 2020; Costa da Silva et al. 2021; Dossa et al. 2022).

Under the influence of the same current system and the ITCZ, the Rocas Atoll represents the only atoll in the South Atlantic. It is located approximately 266 km off the Brazilian coast and about 150 km west of the Fernando de Noronha Archipelago. With an ellipsoidal shape and an approximate area of 5.5 km², the reef system is composed of coralline algae, gastropods, and foraminifera. The atoll is situated atop a seamount at a depth of approximately 4000 m and is part of the Fernando de Noronha Fracture Zone (Longo et al. 2015; Claudino-Sales et al. 2018).

The high biodiversity that characterizes both regions, including the presence of endemic species, is directly related to physical processes, making the area important for marine conservation and scientific research (Claudino-Sales et al. 2019; Matheus et al. 2019).

From historical analysis of satellite altimetry, the cSEC branch appears to have intensified during April-May-June (Dimoune et al. 2023). This also appears in the G12V1 ocean reanalysis seasonal climatology. The meridional vertical section across the Rocas Atoll (Fig. 3) shows that the cSEC branches north and south of the islands are intensified in April-May-June, with a warmer mixed layer. Below 100-m-depth, the southern side is dominated all year long by the eastward SEUC, stronger from July to December, with a subsequent vertical shear. The same vertical patterns occur across the Fernando de Noronha islands (blue section in Fig. 1, not shown). For both islands, the signature of the SEUC also appears north of the islands during April-May-June, as observed by the Abraços campaigns (Costa da Silva at al. 2021).

The Fig. 4, zonal vertical section at the latitude of the islands (black section in Fig. 1) from the G12V1 climatology, shows all along the year the signature of the NBUC in the thermocline, whose eastward extension reaches Rocas Atoll. It is shallower and intensified in April-May-June, as seen also during the Fall 2017 Abraços campaign (Dossa et al., 2021).

Despite the relevance of these physical processes, their observational characterization has historically been limited by data availability and spatial resolution (Dossa et al. 2022). Prior to the availability of SWOT data, the description of the dynamics around Fernando de Noronha and the Rocas Atoll relied primarily on satellite observations of surface parameters such as sea surface temperature, sea surface salinity, sea surface height, and chlorophyll-a, as well as dedicated in situ campaigns like Abraços 1 and 2, which documented the full water-column dynamics over relatively short periods. In parallel, operational oceanography based on numerical models that assimilate available observations has provided continuous three-dimensional representations of the regional circulation. However, none of these approaches resolve spatial scales smaller than approximately 10 km (Le Traon et al. 2025).

4. Methodology

We used version 3.6.1 of the py-eddy-tracker (PET) algorithm to identify and track eddies around the islands of Fernando de Noronha and the Rocas Atoll. The algorithm performs detection based on sea surface height anomalies (SSHA) values and geostrophic velocity anomalies, which were computed relative to a reference climatological period spanning 1993–2012. Widely used in the literature, this routine has been applied in several studies to identify mesoscale eddies (Mason et al. 2014; Mason et al. 2017; Pegliasco et al. 2022). More recently, PET has also been employed for the detection of submesoscale eddies, including applications using SWOT data (Cao et al. 2025; Du and Jung 2025; Ma et al. 2025; Zhang et al. 2025).

In this study, PET was applied to conventional altimetry data (DUACS/MIOST), the G12V1 reanalysis, and the SWOT Level-3 version 3.0 product. The period selected for analysis was from August 2023 to July 2024, corresponding to one year since the beginning of the SWOT science phase.

PET improves detection capability by emphasizing extreme SSHA values. Accordingly, the algorithm begins with the application of a 5° × 5° box filter to the daily SSH data in order to enhance the signal. In the subsequent steps, differences were adopted in the criteria applied to SWOT data and to the other datasets.

For SWOT data, the eddy identification function designed for irregular datasets was applied in order to avoid errors associated with data interpolation. Orbital passes 87 (Rocas Atoll) and 365 (Fernando de Noronha) were selected for data acquisition, as they were located approximately within the 20 km gap between the KaRIn interferometric swaths. This configuration allowed the analysis of circulation both upstream and downstream of the islands.

From these orbital passes, filtered SSHA data were extracted, and the corresponding geostrophic currents anomalies derived from SSHA were used. The procedure for estimating these currents, which incorporates a 2D spline filtering technique, is described in Tranchant et al. (2025), while the method used to filter random noise is presented in Treboutte et al. (2023). According to the SWOT Science Team (https://www.aviso.altimetry.fr), version 3 includes improvements in calibration, tidal correction and noise reduction without removing geostrophic or ageostrophic motions, in addition to enhancing data quality near complex coastal areas in comparison to previous SWOT data versions.

In the subsequent steps of PET execution, SSHA contours ranging from − 100 to 100 cm were identified, with a minimum spacing of 0.05 cm between isolines. Open contours were discarded, whereas closed contours are evaluated according to their shape. In this step, the shape error must be lower than 55%. The error corresponds to the sum of the deviations of the closed contour from a fitted circle relative to the area of that circle.

Another important criterion concerns the minimum and maximum number of pixels considered by the algorithm in the identification of closed contours. For SWOT data, a minimum threshold of 8 pixels and a maximum of 3600 pixels were adopted, corresponding approximately to a detectable size range between 7 km and 60 km. In the context of this study, both Fernando de Noronha and the Rocas Atoll have diameters smaller than 10 km, which may influence the generation of eddies of comparable dimensions.

In addition, Wang et al. (2019) indicated that the sensor resolves spatial scales on the order of 15 km at low latitudes, while Zhang et al. (2025) reported the possibility of detecting eddies from SWOT data with radii between 2 and 7 km.

For the other datasets, whose spatial resolution is at least four times coarser than that of SWOT, SLA and geostrophic current anomalies were used as the input variable for G12V1 and the conventional altimetry products (DUACS/MIOST). Regarding the detection criteria, the tolerable shape error was maintained (< 55%), as well as the maximum number of pixels considered in the eddy detection process.

However, following a strategy similar to that of Du and Jing (2024), without imposing a minimum pixel threshold for eddy detection, given that the focus of this study is the submesoscale. Another

modification consisted of adopting a minimum spacing of 0.1 cm between isolines in order to avoid detecting instrumental noise as real physical structures (Zhang et al. 2025).

After detecting eddies from the different datasets, days exhibiting vortices potentially associated with the Island Mass Effect were identified based on their characteristics (e.g. geostrophic current field pattern) and proximity to the islands. For these days, chlorophyll-*a* concentrations downstream of the islands were examined using Copernicus-GlobColour (4 km) and OLCI (300 m) data. In this study, a threshold of 0.2 mg m^{-3} was adopted to identify events of elevated primary productivity near the islands (Raja and Rosell-Melé, 2021).

In addition, vertical motions near the islands were inferred from the calculation of the second derivative of SST (Laplacian) in order to identify local variations in surface temperature in the vicinity of the islands. According to De Falco et al. (2022), the Laplacian highlights small-scale patterns relative to the large-scale background, allowing the inference of vertical advection processes. The authors further note that strongly positive (negative) Laplacian values correspond to areas of negative (positive) curvature in the temperature field, as observed in regions surrounding a local cold (warm) anomaly relative to the large-scale field.

In order to further characterize the flow regime associated with these processes, the dynamical stability of the ocean flow as it interacts with Fernando de Noronha and Rocas Atoll, the Reynolds number (Re) was calculated. This parameter determines whether the wake generated by a topographic obstacle is laminar or turbulent. The calculation followed the classical formulation for a cylindrical obstacle in a horizontal fluid:

$$Re = \frac{U_0 \cdot D}{A_h}$$

1

where U_0 represents the incident current velocity (in m s^{-1}), corresponding to the large-scale flow in the region, such as the central South Equatorial Current (cSEC). D is the diameter of the obstacle (in meters), defined as the width of the island or atoll perpendicular to the predominant flow direction. A is the horizontal turbulent viscosity coefficient (in m^2 s^{-1}). In this study, a parameterized value of 100 m^2 s^{-1} was adopted, following the recommendations of Sangrà et al. (2007) and De Falco et al. (2022) for studies of current–island interaction in deep waters.

To assess whether events of elevated productivity and vortex activity near the islands are recurrent and systematically detectable, the characteristics of the eddies (location, radius, amplitude, and rotation sense) were analyzed over the entire period (Aug/2023–Aug/2024). In this context, the frequency distribution of eddy characteristics was also evaluated in order to compare the detection capability of the different datasets using PET.

In this study, all eddies located within a radius of 60 km from the center of each island were considered as the spatial sampling domain. This value also corresponds to the threshold between mesoscale and submesoscale adopted by Cao et al. (2025) for latitudes between 5°S and 5°N. The scientific basis for defining the submesoscale considers that eddy diameter is comparable to the baroclinic Rossby radius of deformation, whose threshold for distinguishing the two scales is on the order of 20–30 km (Zhang Y. et al. 2019; Morvan et al. 2020; Ernst et al. 2023). However, these studies are generally conducted at mid-latitudes. At the equator, the Rossby radius of deformation increases significantly, potentially reaching values between 115 km and 250 km.

5. Results and Discussions

5.1 Detection of submesoscale signatures and Island Mass Effect

The initial characterization of ocean dynamics around the Rocas Atoll (AR) and the Fernando de Noronha Archipelago (FN) was based on SSHA and geostrophic currents derived from SWOT data. Over the period from August 2023 to July 2024, multiple snapshots revealed coherent structures consistent with cyclonic and anticyclonic eddy-like features located both upstream and downstream of the islands. These observations are consistent with previous inferences regarding eddy activity in the region (Dossa et al. 2022; Lira et al. 2024), but here they are directly resolved at finer spatial scales.

Figures 5 and 6 illustrate representative cases for AR (04/09/2023) and FN (02/07/2024), respectively. In both cases, the detected structures exhibit closed and approximately circular contours, with dynamical signatures characteristic of fine-scale features: cyclonic (anticyclonic) structures are associated with minimum (maximum) SSHA values at their core and maximum (minimum) values along their outer boundary. Most of these structures present effective radii smaller than 15 km (see Section 5.3).

For the Rocas Atoll case (Fig. 5a), at least three cyclonic eddy-like structures can be identified within the area shown, located to the southwest, northwest, and north of the island. The northern structure is only partially resolved, likely due to its proximity to the nadir gap of the SWOT ascending pass 87. In addition, a small anticyclonic eddy-like structure is observed to the southwest of the atoll. In this snapshot, these structures occur in regions where negative SST anomalies are observed, reaching up to 1°C below the local daily climatology, together with enhanced chlorophyll-a concentration in the southwestern sector of the atoll (Fig. 5c).

The spatial co-occurrence of cyclonic eddy-like structures, cold SST anomalies, and increased chlorophyll concentration suggests the action of submesoscale-driven upwelling processes. In this configuration, eddy circulation promotes the uplift of nutrient-rich South Atlantic Central Water (SACW) toward the euphotic layer, supplying nutrients that enhance primary productivity, as suggested by Cordeiro et al. (2013). According to Archer et al. (2025), submesoscale vortices are characterized by intense gradients and significant vertical velocities (w), which modulate exchanges between the upper

and deeper ocean. In addition, this mechanism is consistent with the interpretation of island-induced enrichment processes described in previous studies (e.g., Zhang et al. 2025) and provides observational support for the Island Mass Effect at fine spatial scales.

Figure 5d presents the SST Laplacian for the Rocas Atoll case. Although a predominantly cold SST anomaly is observed, the Laplacian reveals a more complex spatial structure, characterized by alternating areas of enhanced and suppressed vertical motion. Physically, the Laplacian operator highlights small-scale temperature patterns by identifying the curvature of the SST field; strong positive values correspond to local cold anomalies (negative curvature), which are often indicative of localized upwelling or intensified vertical mixing that brings deeper, colder water to the surface. By using this metric, small-scale variations associated with island dynamics are isolated from the large-scale latitudinal background signal (De Falco et al. 2022).

The anticyclonic vortex near the atoll (Fig. 5d) exhibits negative Laplacian values at its core, likely associated with a region of subsidence, consistent with the expected behavior of anticyclonic vortices, which tend to suppress upwelling (Sangrà et al. 2007). However, regions favorable to upwelling, identified by positive Laplacian signatures, are observed along the vortex periphery. According to De Falco et al. (2022) and other authors, submesoscale ageostrophic processes can generate perturbations in vertical velocity that reverse the traditional geostrophic prediction of downwelling in anticyclones.

Continuing in Fig. 5d, the cyclonic vortices exhibit regions where upwelling is favored and others where it is inhibited, consistent with the findings of McGillicuddy (2016). Within the eddy stirring and eddy-induced Ekman pumping framework, dipole or monopole patterns of vertical velocity may emerge depending on the interaction between surface stress and the horizontal eddy vorticity gradient, generating dipole-like signatures of upwelling and downwelling at eddy boundaries. This indicates that, despite the overall SST cooling observed on 04/09/2023, vertical exchanges are not spatially uniform but are influenced by submesoscale dynamics.

A similar configuration is observed around Fernando de Noronha on 02/07/2024 (Fig. 6), with a spatial alignment between dynamical, thermal, and biogeochemical fields. A well-defined cyclonic eddy-like structure is located downstream of the island, with a clearly identifiable core marked by minimum SSHA values. The associated cold SST anomaly is distributed along the eddy outer boundary, while increased chlorophyll concentration is observed in regions corresponding to these colder waters, particularly in the northwestern sector of the island.

Consistent with the Rocas Atoll case, the SST Laplacian highlights an alternation between regions of enhanced and suppressed upwelling, indicating spatial variability in vertical exchanges. However, in this case, the regions of negative SST anomalies, Laplacian-derived upwelling, and increased chlorophyll concentration largely coincide spatially. This spatial alignment reinforces the link between submesoscale dynamics and biological response in the vicinity of the island.

This result contrasts with that reported by Tchamabi et al. (2017) and Costa da Silva et al. (2021), who suggested that, in Fernando de Noronha, the cooling associated with topographic upwelling often occurs at the base of the mixed layer and may not reach the surface as clearly as chlorophyll signals due to thermal stratification.

5.1.1 Large-scale circulation and limitations of conventional datasets

The large-scale ocean circulation around the islands is shown in Fig. 7 for the two snapshots analyzed, based on geostrophic currents derived from MIOST (red and magenta vectors), superimposed with the G12V1 first level velocity field (black and blue vectors).

Around the Rocas Atoll (04/09/2023), a north–northeastward flow is identified in the DUACS/MIOST fields (Fig. 7a) and is also observed at the edges (34.2 °W and 33.2 °W) of the SWOT swaths (Fig. 5a). East of FN, this flow bifurcates northward, feeding the western edge of a large cyclonic pattern centred at 28°W/2.5°S. This pattern indicates a recirculation of the central branch of the South Equatorial Current (cSEC) in the vicinity of the islands, starting to shift northward around 33°W, consistent with previous studies (Silveira et al. 1994; Dossa et al. 2022). Between 01/09/2023 and 15/10/2023, the cSEC recirculation exhibits an eastward component extending to approximately 25°W, before returning to its typical westward flow (results not shown).

Also on 04/09/2023 (Fig. 7a), the mesoscale cyclonic eddy centred at this date near 28°W likely contributes to modifying the flow in the vicinity of the islands. This observation reinforces the findings of Dossa et al. (2022), who show that the region between 6°S and 2°S is dominated by large cyclonic eddies linked to negative wind curl, contributing to the modulation of the regional circulation.

A comparison between conventional altimetry products and SWOT for the Rocas Atoll case on 04/09/2023 highlights the limitations of these datasets in resolving fine-scale structures. The DUACS/MIOST product does not resolve the complexity of small-scale structures in the region, as submesoscale features are smoothed during the transformation of one-dimensional measurements into gridded fields (Du and Jing, 2024). In addition, at low latitudes, gridded products typically exhibit larger errors due to complex dynamical structures and the wider spacing between conventional satellite tracks (Zhang et al., 2024).

Extending this comparison to G12V1, although it is an eddy-resolving reanalysis, it is also unable to capture the submesoscale eddies near the Rocas Atoll, as it relies on conventional altimetry data that do not resolve high-frequency variability or small-scale features. The local circulation does not appear (Rocas Atoll – 04/09/2023), although, the 1-Hz SWOT nadir SSHA for that day exhibits shorter scale patterns that are filtered out when used to build the MIOST map (note that SWOT data are not assimilated in the G12V1 reanalysis). However, the reanalysis captures large-scale circulation patterns and mesoscale eddies in the analyzed case.

For the Fernando de Noronha case on 02/07/2024 (Fig. 7b), the large-scale circulation follows the typical westward flow of the cSEC and is well represented by DUACS/MIOST. Neither MIOST nor G12V1 capture submesoscale vortices near the island, in contrast to the structures observed in the SWOT data. In this case, while SWOT highlights submesoscale variability, the large-scale circulation pattern is less clearly represented. As a result, and in contrast to the Rocas Atoll case, the flow in the vicinity of Fernando de Noronha appears to be more strongly modulated by submesoscale processes in this snapshot, although these processes likely remain embedded within the large-scale cSEC circulation.

5.2 Eddy field characteristics and spatial distribution

The selected snapshots reveal the complexity of the processes acting in the study region, including variability in the South Equatorial Current and the presence of mesoscale eddies. The interaction between the flow and the islands may also modulate the size and spatial distribution of eddies. To further assess the recurrence and spatial organization of these features, we analyzed the distribution of eddies identified using the py-eddy-tracker (PET) algorithm.

During the period from August 2023 to July 2024, a total of 36 cyclonic and 34 anticyclonic vortices were detected within a 60 km radius of the Rocas Atoll using the py-eddy-tracker algorithm applied to 15 SWOT images from ascending pass 87. In the case of the Fernando de Noronha Archipelago, 19 images from ascending pass 365 were analyzed, resulting in the identification of 63 cyclonic and 52 anticyclonic vortices over the same period.

The spatial distribution of these structures (Fig. 8), which represents the cumulative positions of eddies over the study period, indicates that the detected eddies are predominantly small-scale features, with no eddies exceeding 15 km in effective radius. These scales align with recent observations in the Northwest Pacific, where SWOT resolved fine-scale structures with equivalent radii between 10 and 20 km (Zhang et al. 2024).

Around the Rocas Atoll (Fig. 8a), although no clear dominance of cyclonic over anticyclonic eddies is observed, there is a noticeable concentration of anticyclonic structures in the northwestern quadrant. Considering the geometry of the atoll, this region likely corresponds to the downstream area relative to the prevailing flow. In contrast, around Fernando de Noronha (Fig. 8b), eddies are more evenly distributed across all quadrants, with a slight predominance of cyclonic structures to the southwest and northwest of the island.

Lira et al. (2024) suggest a tendency for cyclonic eddies to occur downstream of the islands. While this pattern is partially observed in Fernando de Noronha, the detection of anticyclonic vortices in downstream regions suggests a more complex local dynamics than previously described.

Despite these localized tendencies, no consistent preferential organization of cyclonic and anticyclonic eddies is observed in the vicinity of the islands, although some of these structures remain visually identifiable. This distribution may instead reflect a predominant eddy-shedding regime, or be associated

with limitations of the PET algorithm in detecting small-radius vortices near the islands, as well as with sampling constraints related to the distance between the SWOT swath and the island location.

To verify if the observed spatial distribution aligns with the physical nature of the wake, the Reynolds number was calculated for each SWOT image near the Rocas Atoll (pass 87) and Fernando de Noronha (pass 365). Mean values of 72 and 95 were obtained, respectively, indicating a possible formation of von Kármán-type eddies in the region. These values align with the theoretical threshold of Re > 50 – 60, where current-island interactions generate unstable wakes and periodic vortex shedding (Heywood et al. 1990; De Falco et al. 2022).

On some days, however, Reynolds numbers below 50 were observed, suggesting conditions favorable for the development of two quasi-stationary, contra-rotating eddies trapped downstream of the islands. Such a “trapped eddy” regime has been documented in similar atoll systems, such as in the oceanic island of Aldabra in the Indian Ocean, where Re values near 30–59 were associated with eddies that did not detach but remained localized in the island’s lee (Heywood et al. 1990). This, in turn, points to a potential transition toward eddy-shedding regimes, depending on the intensity of the westward-flowing cSEC, which acts as the primary topographic forcing in the region.

The higher mean Reynolds number at FN compared to AR indicates that the archipelago induces more persistent and turbulent wake instabilities, consistent with high-resolution numerical simulations of the Fernando de Noronha ridge (Tchamabi et al. 2017). This is further supported by the monthly distribution of vortices (Fig. 9), normalized by the number of observation days, which shows that, except for February 2024, the number of vortices detected around Fernando de Noronha is consistently higher than around the Rocas Atoll.

This difference can be attributed to the greater topographic complexity and size of FN (26 km²; 323 m elevation) compared to AR (0.36 km²; 6 m elevation) (Tchamabi et al. 2017). As a larger obstacle, FN induces more significant perturbations in the central South Equatorial Current (cSEC), including upstream core splitting and more frequent unstable wake regimes (Costa da Silva et al. 2021). However, the role of seasonal fluctuations in cSEC intensity can not be ignored.

In order to infer the possible contribution of the cSEC branch intensity and direction crossing the islands, box averaged statistics of the G12V1 velocity at the surface are carried out over 4 areas: north, south, east and west of Fernando de Noronha archipelago and Rocas Atoll. Results over the four boxes, around the two islands, are very similar for zonal and also meridional velocities, the reason why we only present here in Figs. 10 and 11 the zonal current east of FdN and the meridional current south of Rocas Atoll. From Fig. 10, we observe that when the zonal current is stronger than − 0.4 m/s, the number of eddies is higher the same or following month in Fig. 9. The meridional component is less intense and there is no visible pattern that could explain the variation of the number of eddies around the islands.

5.4 Detection capability: SWOT vs conventional datasets

This section evaluates the capability of conventional altimetric products and SWOT to detect submesoscale eddies around the islands, based on their effective radius and amplitude as identified by the PET algorithm within a 60 km (submesoscale threshold) radius.

In terms of effective radius (Fig. 12a), the eddies detectable by DUACS/MIOST exhibited radii greater than 30 km, while G12V1 identified eddies with radii exceeding 16 km. Although these radii are typical of submesoscale eddies in the equatorial region, only SWOT was able to characterize the fine-scale dynamics around the islands, detecting eddies with radii as small as 3 km. This is consistent with a recent study by Zhang et al. (2025), which identified submesoscale eddies with radii ranging from 2 to 8 km in the Northwest Pacific using the PET algorithm as a detection method.

As demonstrated by Coadou-Chaventon et al. (2025) and Archer et al. (2025), the high spatial resolution and low noise floor of SWOT allow it to resolve SSH gradients associated with dynamics where the geostrophic approximation is no longer strictly valid ($Ro \gtrsim 1$). Consequently, the SWOT SSH offers gradients that might correspond to real ageostrophic signal, such as centrifugal accelerations in compact vortices and unbalanced motions like internal solitary waves, the latter not fully removed by the new corrections afforded by the SWOT science team. These signals bring real representation of SSH at finer scale.

Regarding amplitude (Fig. 12b), a dominance of structures with peaks between 0.2 and 0.6 cm is observed. According to Douglass and Richman (2015), eddies near the equator can be highly circular, however most of them exhibit very small amplitudes.

Over the analysed period, applying a mesoscale eddy criterion of at least 1 cm in amplitude would have excluded most of the features identified in this study by conventional datasets. This is because structures weaker than 1 cm are typically categorized as noisy artifacts or filtered out during the objective analysis of gridded products (Pegliasco et al. 2015). These results reflect the low density of high-amplitude eddies in the region, a characteristic previously reported by Dossa et al. (2022), who noted that the near-equatorial Atlantic requires advanced observational capabilities to capture low-amplitude geostrophic features. It is possible that eddies detected by conventional datasets would be transient features, such as signatures of tropical waves of different types, which are not adequately represented in Level-4 products.

It is also worth noting that, despite their low amplitude, the vortices detected by SWOT are unlikely to be noise. Studies such as Fu et al. (2024) and Dibarboure et al. (2025) indicate that the standard deviation of instrumental noise in the 2 km data product is approximately 0.4 cm. Furthermore, the use of Level 3 expert products ensures that random errors are mitigated through advanced AI-based denoising algorithms (U-Net architecture), specifically designed to suppress noise while preserving physically meaningful kilometer-scale oceanic structures (Tréboutte et al., 2023). Additionally, for the analyzed period, SWOT exhibits a broader distribution of detected amplitudes compared to the other datasets, also identifying more energetic events with amplitudes of up to 2 cm.

6. Conclusion

This study demonstrates that island-induced dynamics associated with the Island Mass Effect generate detectable surface signatures at submesoscale scales around small oceanic islands when observed with sufficient resolution. Using SWOT data, eddies with radii as small as ~ 3 km and amplitudes well below 1 cm were consistently identified around the Fernando de Noronha Archipelago and the Rocas Atoll. These features are not resolved by conventional altimetric products or reanalyses, indicating that their apparent absence reflects observational limitations rather than physical processes. However, global operational systems such as those of Mercator Ocean, which developed G12V1 distributed by Copernicus Marine, offer horizontal resolutions of 5–7 km in the tropical band, which should enable the dynamic representation of the eddy fields with diameters of 15 km or less, in the vicinity of islands or in shelf seas. This presents new challenges in terms of assimilating SWOT data into these operational systems to enable them to represent the fine-scale mesoscale ocean.

Beyond detection, the results show that island–flow interactions in the tropical Atlantic are dominated by submesoscale variability embedded within larger-scale circulation, with a predominant eddy-shedding regime modulated by the intensity of the central South Equatorial Current (cSEC) and island geometry. This challenges the conventional view derived from coarse-resolution datasets, which underestimate both the frequency and spatial organization of eddies in near-equatorial regions, and helps bridge a key observational gap in the understanding of fine-scale circulation in insular environments.

The spatial alignment between eddy structures, thermal anomalies, and chlorophyll-a distributions suggests that submesoscale dynamics contribute to vertical exchanges and biological productivity around oceanic islands. This has implications for the monitoring and prediction of ecosystem responses in regions where localized physical processes drive biogeochemical variability, and may support ecosystem-based management and the sustainable use of marine resources in island-influenced systems.

Some limitations remain. The temporal sampling of SWOT and the use of the PET algorithm introduce uncertainties, particularly near the coastline, and vertical processes are inferred indirectly from surface diagnostics. The continuity of SSH fields and the integration of satellite observations with in situ data and high-resolution models remain important challenges. In this context, recent developments in conventional altimetry, providing along-track products at 5 Hz (~ 1.5 km resolution) and 20 Hz (< 300 m resolution), should also be considered in combination with SWOT KaRIn data to improve temporal coverage.

In addition, methods such as VarDyn and 4DVar have advanced SWOT data reconstruction (Le Guillou et al. 2025; Zhang et al. 2025), however they have been mainly applied to mid-latitude regions where the quasi-geostrophic (QG) approximation is valid, and their applicability in equatorial regions remains uncertain. Investigating these approaches in equatorial environments represents an important direction for future work. Extending time series will be essential to better resolve island-induced dynamics and quantify the impact of submesoscale processes on marine ecosystems.

Declarations

Acknowledgements

Diógenes Passos Fontenele acknowledges the support of EOLLAB/LABOMAR and FUNCEME in the development of this research. Fabrice Hernandez contributed to this work with the support of the SWOT-SWATI project funded by the CNES/TOSCA program (grant number 4500083699), which also contributes to the verification and validation of operational products at Mercator Océan. The last author, Eduardo Sávio P. R. Martins, acknowledges support from the CAPES-COFECUB grant no. 88887.711963/2022-00 (Call 32/2022) and from the FUNCAP-FIT grant 4920881/2018.

Author contributions

All authors contributed to the initial definition of this work. Satellite and model data collection, and analysis were performed by Diógenes Passos Fontenele and Fabrice Hernandez. The first draft of the manuscript was written by Diógenes Passos Fontenele and Fabrice Hernandez, with corrections and editing by Antonio Geraldo Ferreira and Eduardo Sávio P. R. Martins. All authors commented on the different versions of the manuscript. All authors read and approved the submitted manuscript. Fabrice Hernandez, Antonio Geraldo Ferreira and Eduardo Sávio P. R. Martins contributed to the funding acquisition that permitted this work.

Financial and competing interests

The authors have no relevant financial or non-financial interests to disclose, and no competing interests to declare that are relevant to the content of this article.

Funding

This work was supported by the Centre National d'Études Spatiales (CNES) through the TOSCA program (SWOT-SWATI project, Grant number 4500083699), the Coordenação de Aperfeiçoamento de Pessoal de Nível Superior (CAPES-COFECUB) (Grant No. 88887.711963/2022-00, Call 32/2022), and the Fundação Cearense de Apoio ao Desenvolvimento Científico e Tecnológico (FUNCAP) through the FIT program (Grant 4920881/2018).

References

1. Alves JMR, Tomé R, Caldeira RMA, Miranda PMA (2021) Asymmetric ocean response to atmospheric forcing in an island wake: A 35-year high-resolution study. Front Mar Sci 8. https://doi.org/10.3389/fmars.2021.624392
2. Amaya DJ, Alexander MA, Scott JD, Jacox MG (2023a) An evaluation of high-resolution ocean reanalyses in the California Current System. Prog Oceanogr 210:102951. https://doi.org/10.1016/j.pocean.2022.102951

3. Amaya DJ, Jacox MG, Alexander MA, Scott JD, Deser C, Capotondi A, Phillips AS (2023b) Bottom marine heatwaves along the continental shelves of North America. Nat Commun 14:1038. https://doi.org/10.1038/s41467-023-36567-0
4. Archer M, Wang J, Klein P, Dibarboure G, Fu LL (2025) Wide-swath satellite altimetry unveils global submesoscale ocean dynamics. Nature 640:691–696. https://doi.org/10.1038/s41586-025-08722-8
5. Ballarotta M et al (2019) On the resolution of ocean altimetry maps. Ocean Sci 15:1091–1109. https://doi.org/10.5194/os-15-1091-2019
6. Ballarotta M et al (2025) Integrating wide-swath altimetry data into Level-4 multi-mission maps. Ocean Sci 21:63–80. https://doi.org/10.5194/os-21-63-2025
7. Birol, F., and Coauthors, (2017). Coastal applications from nadir altimetry: Example of the X-TRACK regional products. Advances in Space Research, 59 (4), 936–953. doi: https://doi.org/10.1016/j.asr.2016.11.005
8. Cao L, Zhang Y, Wang Y, Hong M, Wei Y, Qiu C, Xia X (2025) Submesoscale eddies identified by SWOT and their comparison with mesoscale eddies in the tropical western Pacific. Remote Sens 17:3242. https://doi.org/10.3390/rs17183242
9. Carli E, Tranchant YT, Siegelman L, Le Guillou F, Morrow R, Ballarotta M, Vergara O (2025) Southern Ocean 3D eddy diagnostics derived from SWOT. J Geophys Res Oceans 130:e2024JC022307. https://doi.org/10.1029/2024JC022307
10. Coadou-Chaventon S, Swart S, Novelli G, Speich S (2025) Resolving sharper fronts of the Agulhas Current Retroflection using SWOT altimetry. Geophys Res Lett 52:e2025GL115203. https://doi.org/10.1029/2025GL115203
11. Cordeiro TA, Brandini FP, Rosa RS, Sassi R (2013) Deep chlorophyll maximum in the western equatorial Atlantic: How does it interact with island slopes and seamounts? Mar Sci 3:30–37. https://doi.org/10.5923/j.ms.20130301.03
12. Costa da Silva A, Chaigneau A, Dossa AN, Eldin G, Araujo M, Bertrand A (2021) Surface circulation and vertical structure of upper ocean variability around Fernando de Noronha Archipelago and Rocas Atoll during spring 2015 and fall 2017. Front Mar Sci 8:598101. https://doi.org/10.3389/fmars.2021.598101
13. De Falco C, Desbiolles F, Bracco A, Pasquero C (2022) Island mass effect: A review of oceanic physical processes. Front Mar Sci 9:894860. https://doi.org/10.3389/fmars.2022.894860
14. Dibarboure G, Anadon C, Briol F, Cadier E, Chevrier R, Delepoulle A, Faugère Y, Laloue A, Morrow R, Picot N, Prandi P, Pujol MI, Raynal M, Tréboutte A, Ubelmann C (2025) Blending 2D topography images from the Surface Water and Ocean Topography (SWOT) mission into the altimeter constellation with the Level-3 multi-mission Data Unification and Altimeter Combination System (DUACS). Ocean Sci 21:283–323. https://doi.org/10.5194/os-21-283-2025
15. Dimoune DM, Birol F, Hernandez F, Léger F, Araujo M (2023) Revisiting the tropical Atlantic western boundary circulation from a 25-year time series of satellite altimetry data. Ocean Sci 19:251–268. https://doi.org/10.5194/os-19-251-2023

16. Dong C, McWilliams JC, Shchepetkin AF (2007) Island wakes in deep water. J Phys Oceanogr 37:962–981. https://doi.org/10.1175/JPO3047.1
17. Dossa AN, Silva AC, Chaigneau A, Eldin G, Araujo M, Bertrand A (2021) Near-surface western boundary circulation off Northeast Brazil. Prog Oceanogr 190:102475. https://doi.org/10.1016/j.pocean.2020.102475
18. Dossa AN, Costa da Silva A, Hernandez F, Aguedjou HMA, Araújo M, Chaigneau A, Bertrand A (2022) Mesoscale eddies in the southwestern tropical Atlantic. Front Mar Sci 9:886617. https://doi.org/10.3389/fmars.2022.886617
19. Doty MS, Oguri M (1956) The island mass effect. J Cons 22:33–37. https://doi.org/10.1093/icesjms/22.1.33
20. Douglass EM, Richman JG (2015) Analysis of ageostrophy in strong surface eddies in the ocean. J Geophys Res Oceans 120:6799–6821. https://doi.org/10.1002/2014JC010350
21. Du T, Jing Z (2024) Fine-scale eddies detected by SWOT in the Kuroshio Extension. Remote Sens 16:3488. https://doi.org/10.3390/rs16183488
22. Fu LL et al (2024) The Surface Water and Ocean Topography mission: A breakthrough in radar remote sensing of the ocean and land surface water. Geophys Res Lett 51:e2023GL107652. https://doi.org/10.1029/2023GL107652
23. Hamner WM, Hauri IR (1981) Effects of island mass: Water flow and plankton pattern around a reef in the Great Barrier Reef lagoon, Australia. Limnol Oceanogr 26:1084–1094. https://doi.org/10.4319/lo.1981.26.6.1084
24. Hasegawa D, Lewis MR, Gangopadhyay A (2009) How islands cause phytoplankton to bloom in their wakes. Geophys Res Lett 36. https://doi.org/10.1029/2009GL039743
25. Jousset, S. et al (2023). New Global Mean Dynamic Topography CNES-CLS-22 Combining Drifters, Hydrological Profiles and High Frequency Radar Data ESS Open Archive, 2023 (1203). doi: doi:10.22541/essoar.170158328.85804859/v1
26. Laurindo LC, Mariano AJ, Lumpkin R (2017) An improved near-surface velocity climatology for the global ocean from drifter observations. Deep Sea Res Part I 124:73–92. https://doi.org/10.1016/j.dsr.2017.04.009
27. Le Guillou F, Chapron B, Rio MH (2025) VarDyn: Dynamical joint-reconstructions of sea surface height and sea surface temperature. J Adv Model Earth Syst 17:e2024MS004689. https://doi.org/10.1029/2024MS004689
28. Lellouche JM et al (2021) The Copernicus Global 1/12° oceanic and sea ice GLORYS12 reanalysis. Front Earth Sci 9:698876. https://doi.org/10.3389/feart.2021.698876
29. Lira SMA, Teixeira IA, Mello de Lima CD, Santos de Souza G, Neumann Leitão S, Schwamborn R (2014) Spatial and nycthemeral distribution of the zooneuston off Fernando de Noronha, Brazil. Braz J Oceanogr 62. https://doi.org/10.1590/s1679-87592014058206201
30. Lira SMA et al (2024) Multiple island effects shape oceanographic processes and zooplankton size spectra off an oceanic archipelago in the Tropical Atlantic. J Mar Syst 242:103942.

https://doi.org/10.1016/j.jmarsys.2023.103942

31. Liu L, Zhang X, Fei J, Li Z, Shi W, Wang H, Jiang X, Zhang Z, Lv X (2023) Key factors for improving the resolution of mapped sea surface height using a two-dimensional variational method. Remote Sens 15:4275
32. Ma C, Xiao G, Di J et al (2020) An investigation of the influences of SWOT sampling and mapping on eddy identification in the Kuroshio Extension. Remote Sens 12:2682. https://doi.org/10.3390/rs12172682
33. McGillicuddy DJ (2016) Mechanisms of physical–biological–biogeochemical interaction at the oceanic mesoscale. Annu Rev Mar Sci 8:125–159. https://doi.org/10.1146/annurev-marine-010814-015606
34. Pegliasco C, Chaigneau A, Morrow R (2015) Main eddy vertical structures observed in the four major Eastern Boundary Upwelling Systems. J Geophys Res Oceans 120:6008–6033. https://doi.org/10.1002/2015JC010950
35. Qiu B, Chen S (2025) Fine-scale upper-ocean variability in the Kuroshio Extension region from the wide-swath SWOT measurements. J Phys Oceanogr 55:2229–2242. https://doi.org/10.1175/JPO-D-25-0042.1
36. Sangrà P, Jiménez B, Hernández-Arencibia M, Marrero-Díaz A, Rodríguez-Santana A, Stegner A, Martínez-Marrero A, Pelegrí JL (2007) The Canary Islands eddy corridor: A major pathway for long-lived eddies in the subtropical North Atlantic. Dyn Atmos Oceans 43:1–25. https://doi.org/10.1016/j.dynatmoce.2007.04.003
37. Shi H, Wu Y, Shi Y, He X, Zheng X, Andersen OB (2025) Enhanced sea surface height estimation with interference rejection using high-frequency fully focused SAR altimetry data over island areas. IEEE Trans Geosci Remote Sens. https://doi.org/10.1109/TGRS.2025.3568079
38. Silveira ICA, Miranda LB, Brown WS (1994) On the origins of the North Brazil Current. J Geophys Res 99:22501–22512. https://doi.org/10.1029/94JC01776
39. Taburet G et al (2019) DUACS DT2018: 25 years of reprocessed sea level altimetry products. Ocean Sci 15:1207–1224. https://doi.org/10.5194/os-15-1207-2019
40. Tchamabi CC, Araujo M, Silva M, Bourlès B (2017) A study of the Brazilian Fernando de Noronha island and Rocas atoll wakes in the tropical Atlantic. Ocean Model 111:9–18. https://doi.org/10.1016/j.ocemod.2016.12.009
41. Teinturier S, Stegner A, Didelle H, Viboud S (2010) Small-scale instabilities of an island wake flow in a rotating shallow-water layer. Dyn Atmos Oceans 49:1–24. https://doi.org/10.1016/j.dynatmoce.2008.10.006
42. Tréboutte A, Carli E, Ballarotta M, Carpentier B, Faugère Y, Dibarboure G (2023) KaRIn noise reduction using a convolutional neural network for the SWOT ocean products. Remote Sens 15:2183. https://doi.org/10.3390/rs15082183
43. Tzortzis R et al (2021) Impact of moderately energetic fine-scale dynamics on the phytoplankton community structure in the western Mediterranean Sea. Biogeosciences 18:6455–6477.

https://doi.org/10.5194/bg-18-6455-2021

44. Verezemskaya P et al (2021) Assessing eddying (1/12°) ocean reanalysis GLORYS12 using the 14-year instrumental record from 59.5°N section in the Atlantic. J Geophys Res Oceans 126:e2020JC016317. https://doi.org/10.1029/2020JC016317
45. Verger-Miralles E et al (2025) SWOT enhances small-scale eddy detection in the Mediterranean Sea. Geophys Res Lett 52:e2025GL116480. https://doi.org/10.1029/2025GL116480
46. Vignudelli S, Birol F, Benveniste J, Fu LL, Picot N, Raynal M, Roinard H (2019) Satellite altimetry measurements of sea level in the coastal zone. Surv Geophys 40:1319–1349. https://doi.org/10.1007/s10712-019-09569-1
47. Zhang L, Hwang C, Liu HY, Chang ETY, Yu D (2025) Automated eddy identification and tracking in the Northwest Pacific based on conventional altimeter and SWOT data. Remote Sens 17:1665
48. Zhang X, et al. (2025) Advances in surface water and ocean topography for fine-scale eddy identification from altimeter sea surface height merging maps in the South China Sea. Ocean Sci 21:1033–1045. https://doi.org/10.5194/os-21-1033-2025
49. Zhang Z, et al. (2024) Submesoscale eddies detected by SWOT and moored observations in the northwestern Pacific. Geophys Res Lett 51:e2024GL110000. https://doi.org/10.1029/2024GL110000

Figures

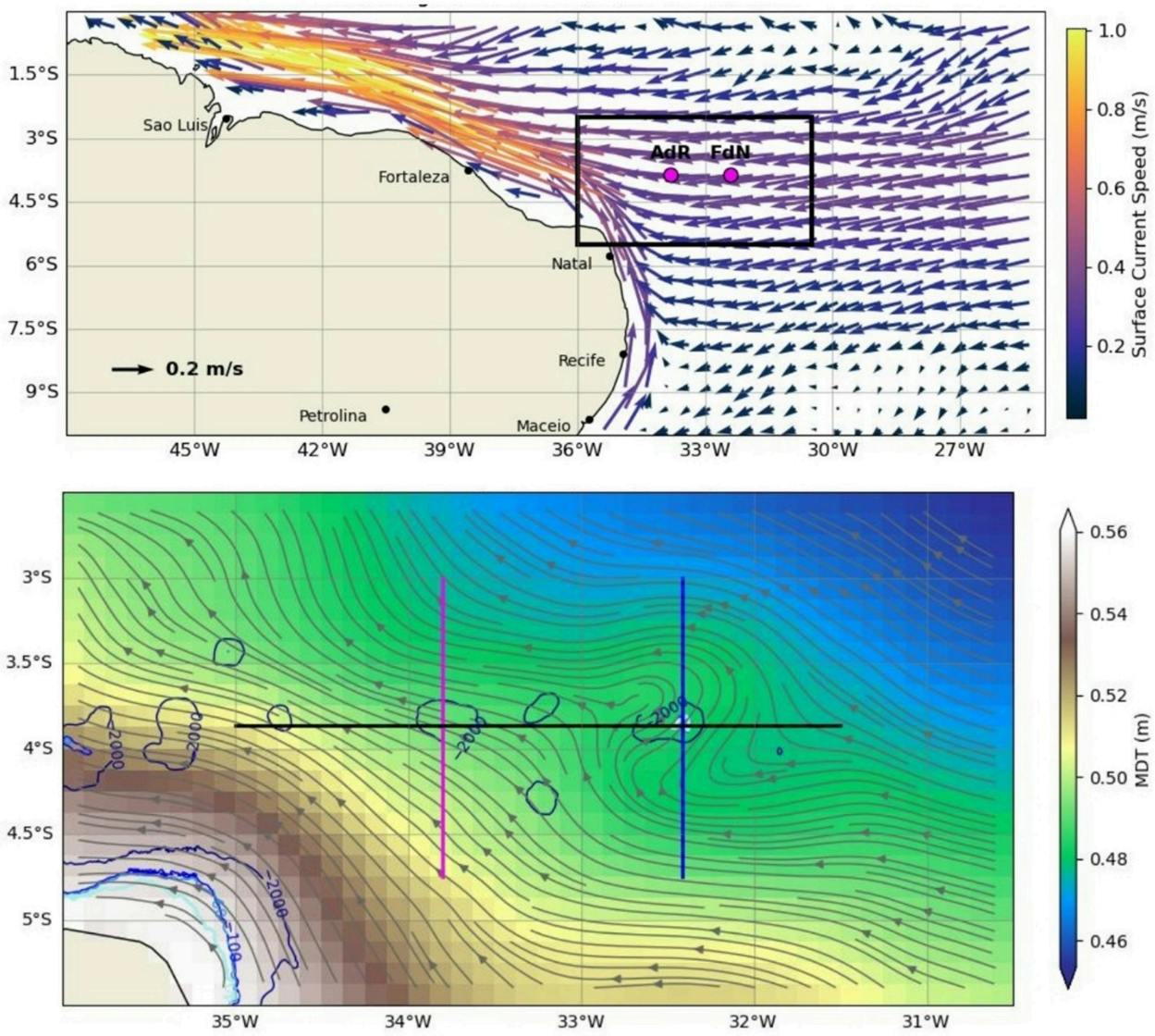


Figure 1

Top: General surface circulation as given by surface drifter velocity climatology (Laurindo et al. 2017). Colored arrows indicate the current intensity (m s^{-1}). The area limited by the black rectangle corresponds to the area of interest. Bottom: Mean Dynamic Topography (m) with streamplots superimposed (Jousset et al., 2023). Magenta, blue and black lines indicate the sections of interest respectively for Rocas Atoll, Fernando de Noronha areas, then a zonal section along the islands

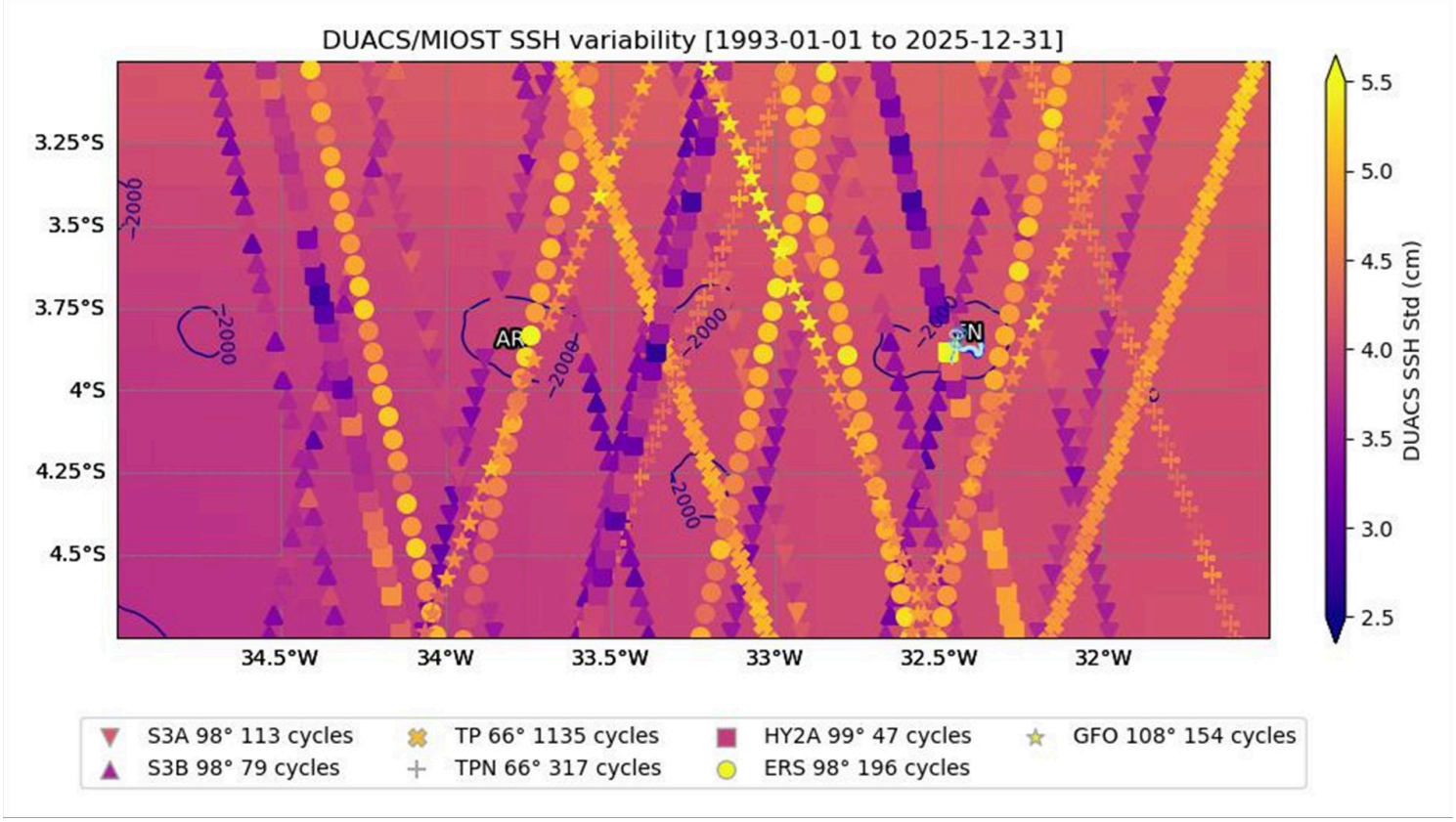


Figure 2

Using the XTRACK 1 Hz nadir altimetry product, illustration of the Sea Level Anomaly (SLA) variability (cm) around the Fernando de Noronha and Rocas Atoll. Data from 1993 to 2025 (missing Cryosat-2 data). Repeat tracks series are represented by different markers, associated satellite orbit inclination and number of repeat cycles used to compute the SLA standard deviations. “TP” groundtracks merges the T/P, Jason-1-2-3 and Sentinel-6 data; “TPN” corresponds to the merging of the interleaved T/P, Jason-1-2-3 missions; “ERS” merges the ERS1-2, EnviSat and Saral/Altika data. The background shaded information corresponds to the standard deviation of the DUACS/MIOST L4 daily products (same colormap in cm)

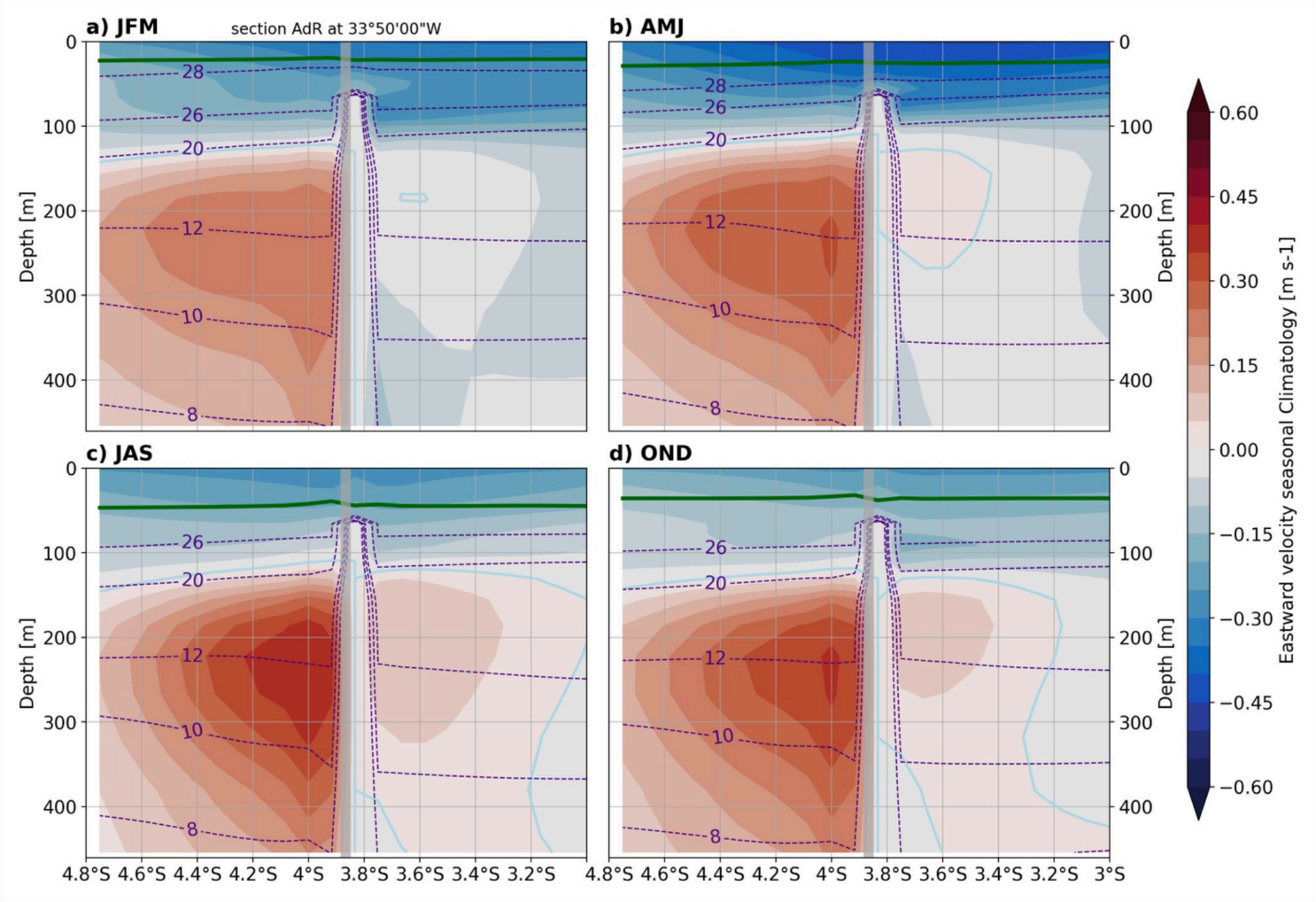


Figure 3

Vertical meridional section at 33°50’W of zonal currents (m s^{-1}) from the G12V1 reanalysis (magenta line in Fig. 1). The position of the Rocas Atoll is given by the vertical gray line. Mixed Layer Depth in green. Isotherms in indigo

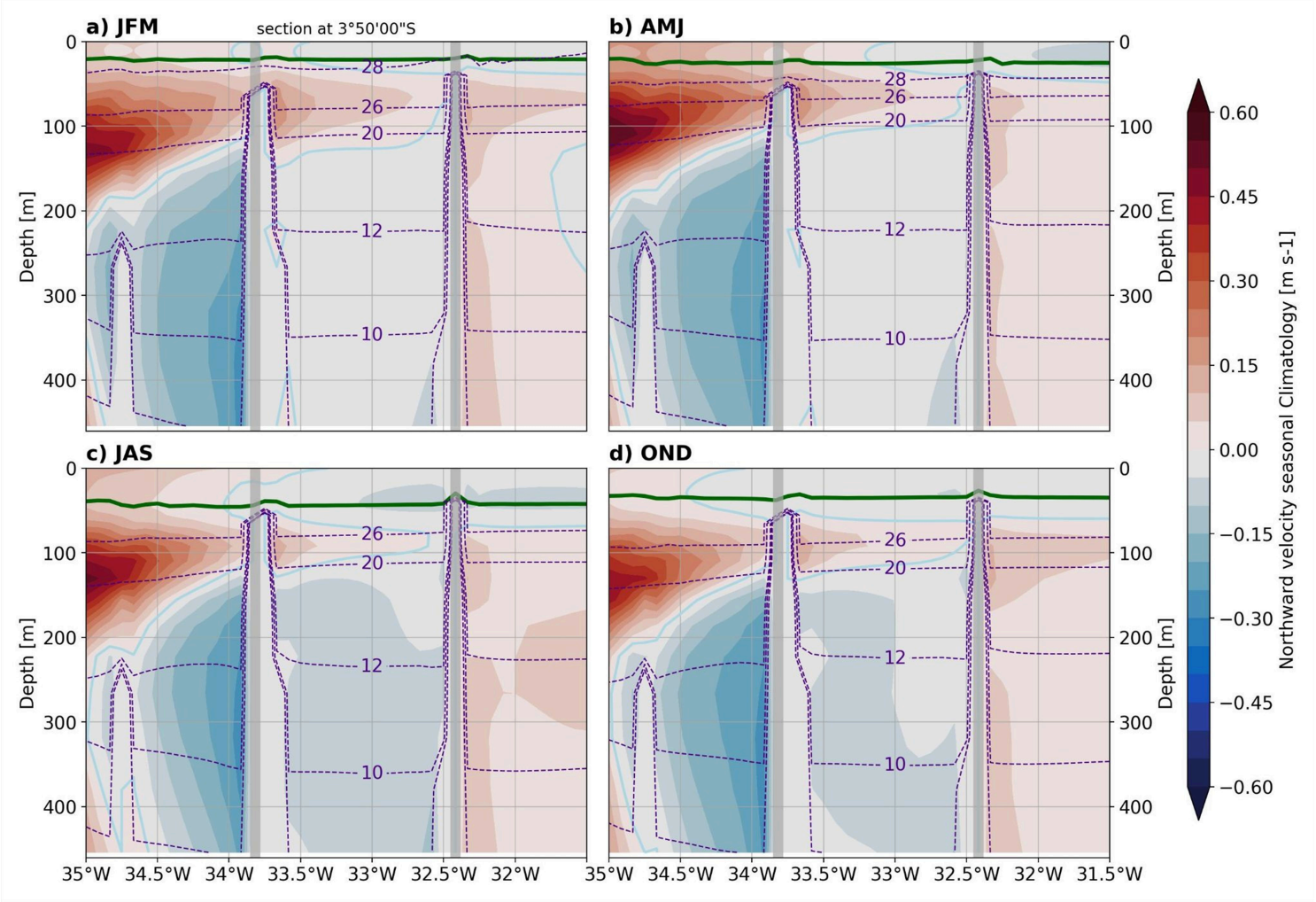


Figure 4

Vertical zonal section at 3°50’S of meridional currents (m s^{-1}, positive northward) from the G12V1 reanalysis (black line in Fig. 1). The position of the Rocas Atoll and Fernando de Noronha archipelago are given by the vertical gray line. Mixed Layer Depth in green. Isotherms in indigo

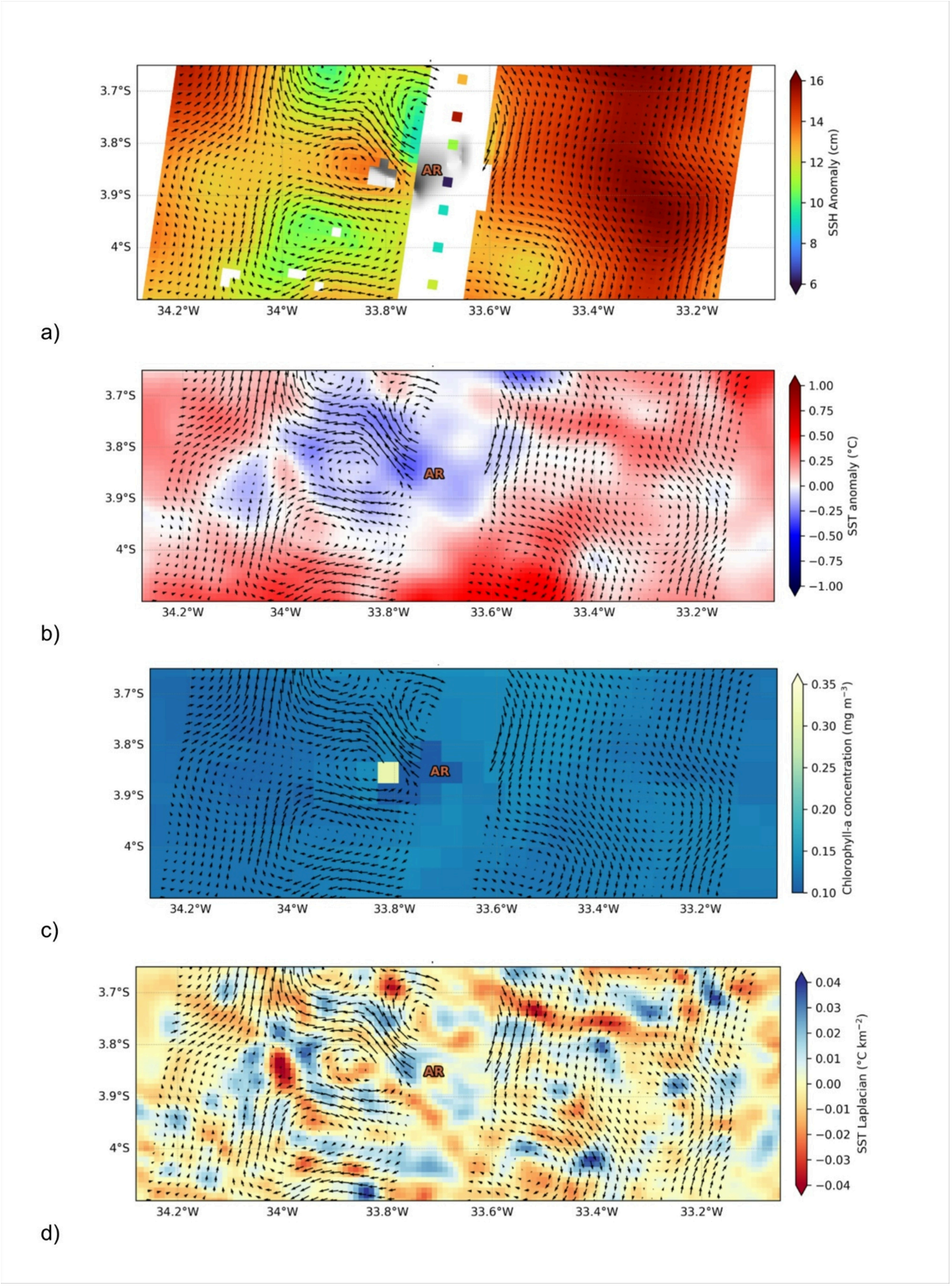


Figure 5

Surface signatures of submesoscale dynamics around the Rocas Atoll on 03/09/2023. (a) Sea Surface Height Anomaly (SSHA, cm), (b) Sea Surface Temperature anomaly (SSTa, °C), (c) Chlorophyll-a concentration (mg m^{-3}), and (d) Laplacian of SST (°C km^{-2}). Geostrophic currents (black arrows) are overlaid in all panels

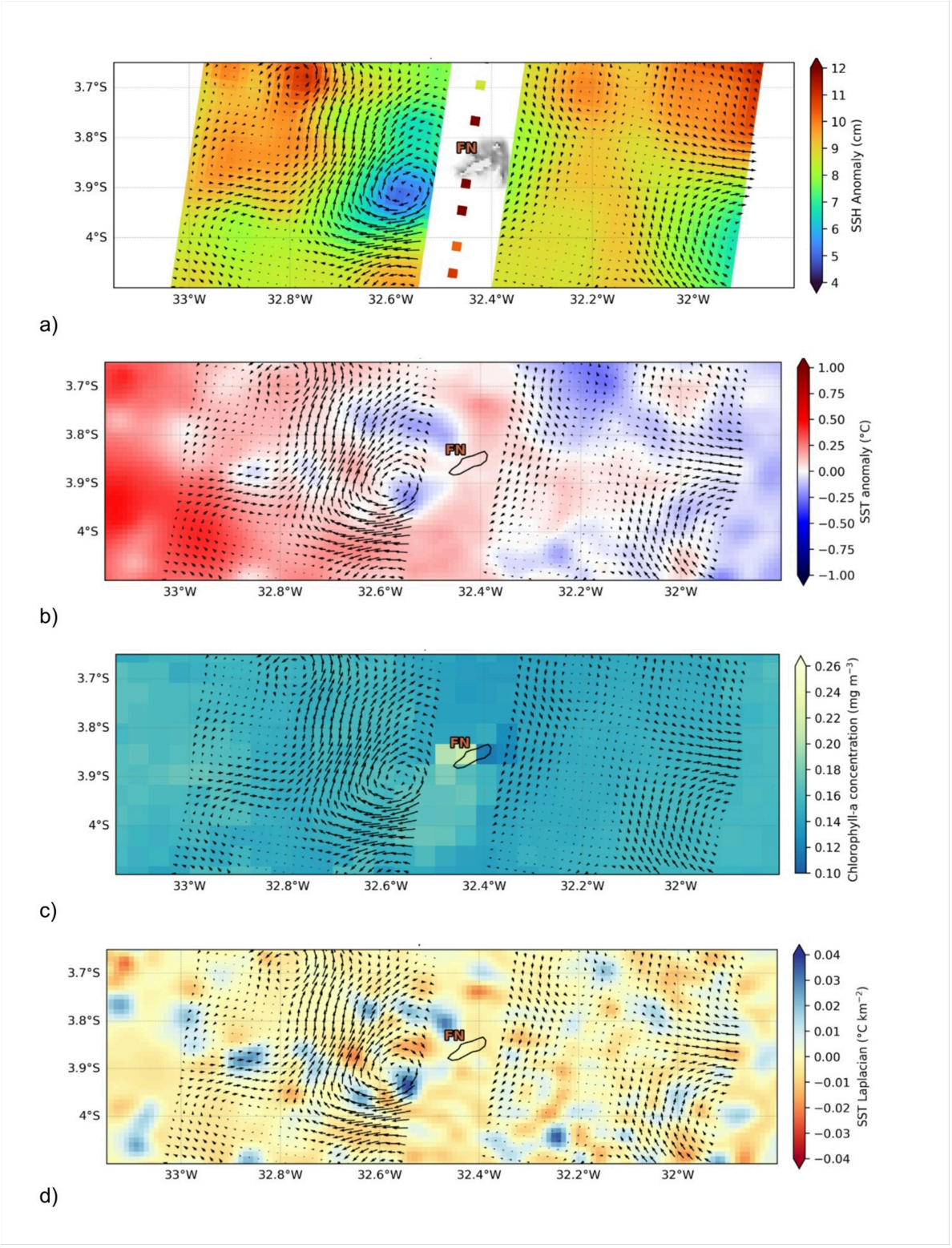


Figure 6

Surface signatures of submesoscale dynamics around the Fernando de Noronha on 02/07/2024. (a) Sea Surface Height Anomaly (SSHA, cm), (b) Sea Surface Temperature anomaly (SSTa, °C), (c) Chlorophyll-a concentration (mg m^{-3}), and (d) Laplacian of SST (°C km^{-2}). Geostrophic currents (black arrows) are overlaid in all panels

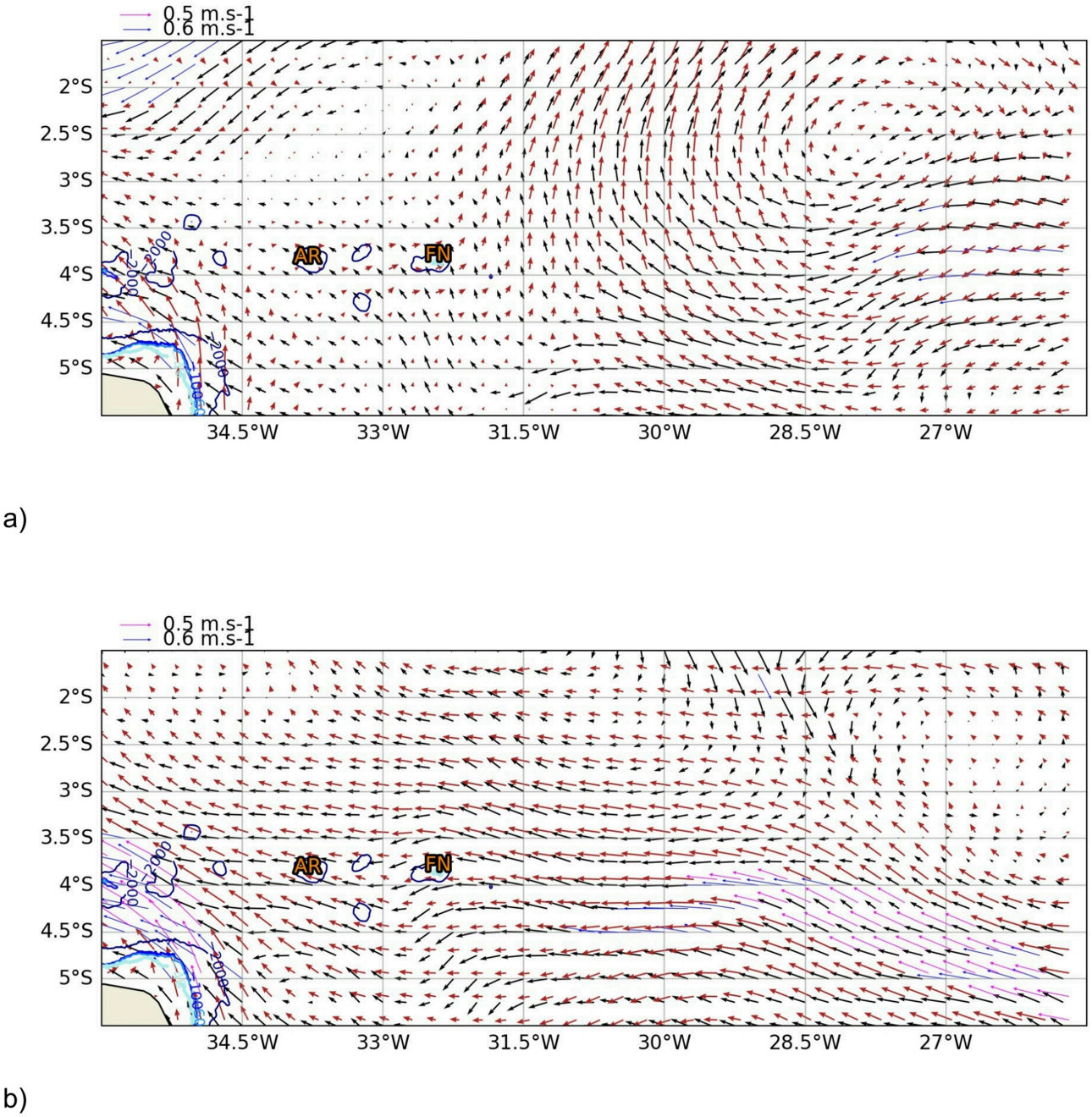


Figure 7

Geostrophic currents from DUACS/MIOST: red and magenta vectors (one vector over two on the 1/8° grid), the scale is given by the magenta vector key on the left top of the figure. Magenta vector drawn for velocities larger than 0.5 m/s). Superimposed, the currents from G12V1 (one every 3 vectors of the 1/12° grid for the sake of clarity): black and blue vectors, the scale represented by the blue vector is chosen smaller because G12V1 provides larger surface velocities. Blue vector drawn for velocities larger than 0.6 m/s. Both fields are highlighting the circulation patterns in the vicinity of the islands for (a) 03/09/2023 and (b) 02/07/2024.

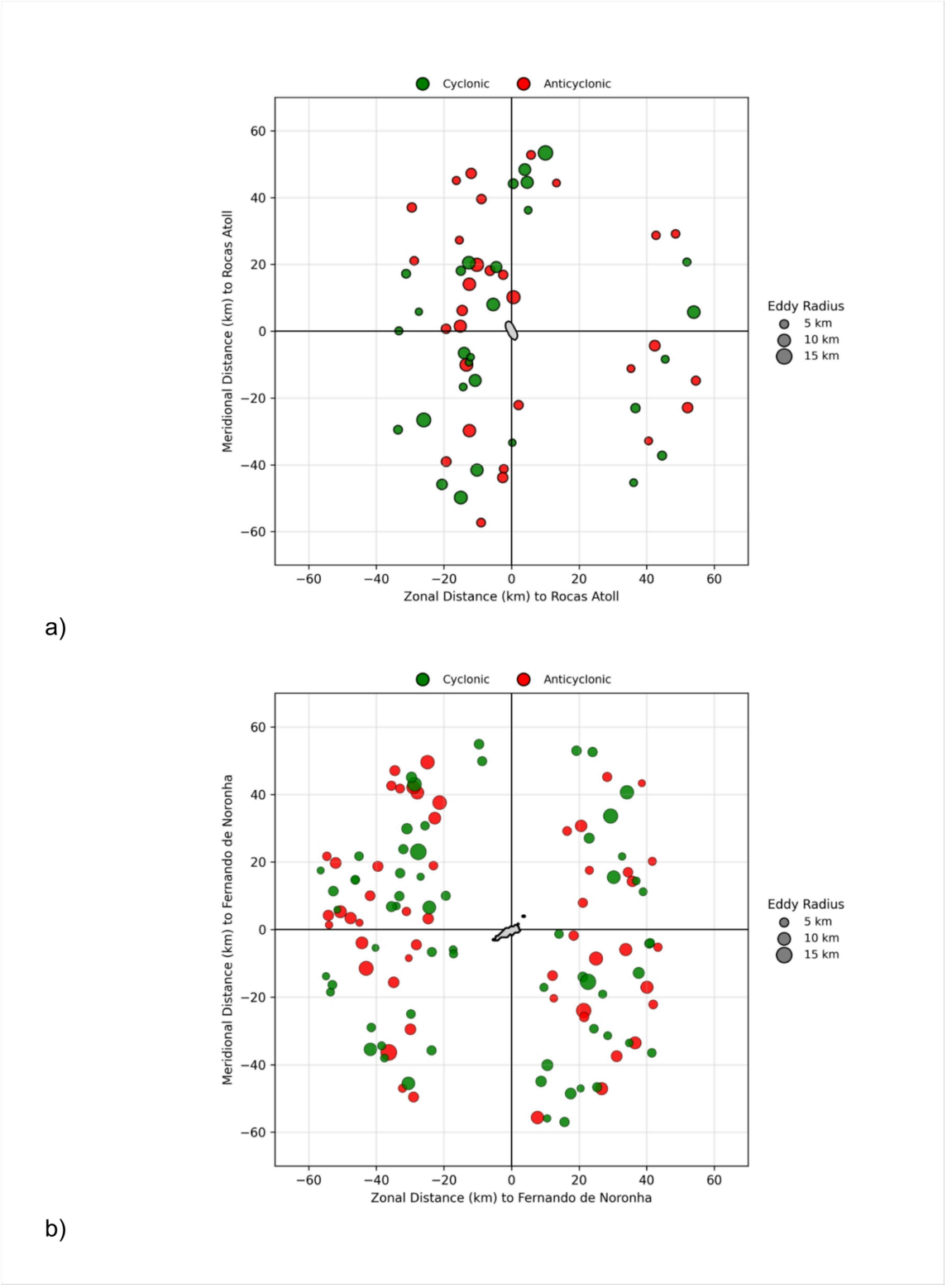


Figure 8

Spatial distribution of cyclonic (green) and anticyclonic (red) eddies within 60 km of the islands from August 2023 to July 2024, shown as a function of effective radius. (a) Rocas Atoll and (b) Fernando de Noronha. Distances are expressed relative to each island in the zonal and meridional directions, and marker size is proportional to eddy effective radius

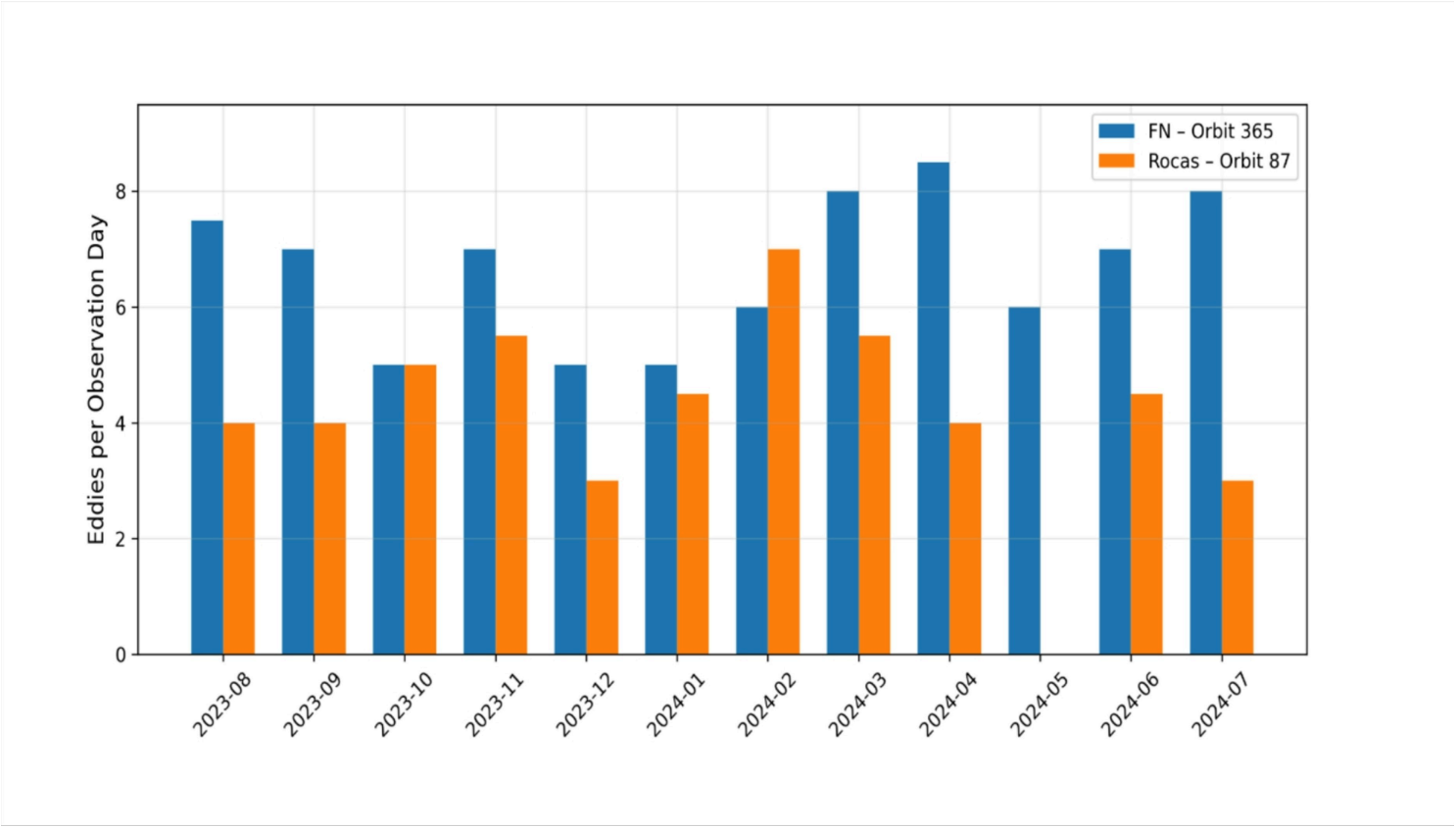


Figure 9

Monthly eddy occurrence normalized by the number of observation days around Fernando de Noronha (FN, pass 365) and the Rocas Atoll (Rocas, pass 87) from August 2023 to July 2024

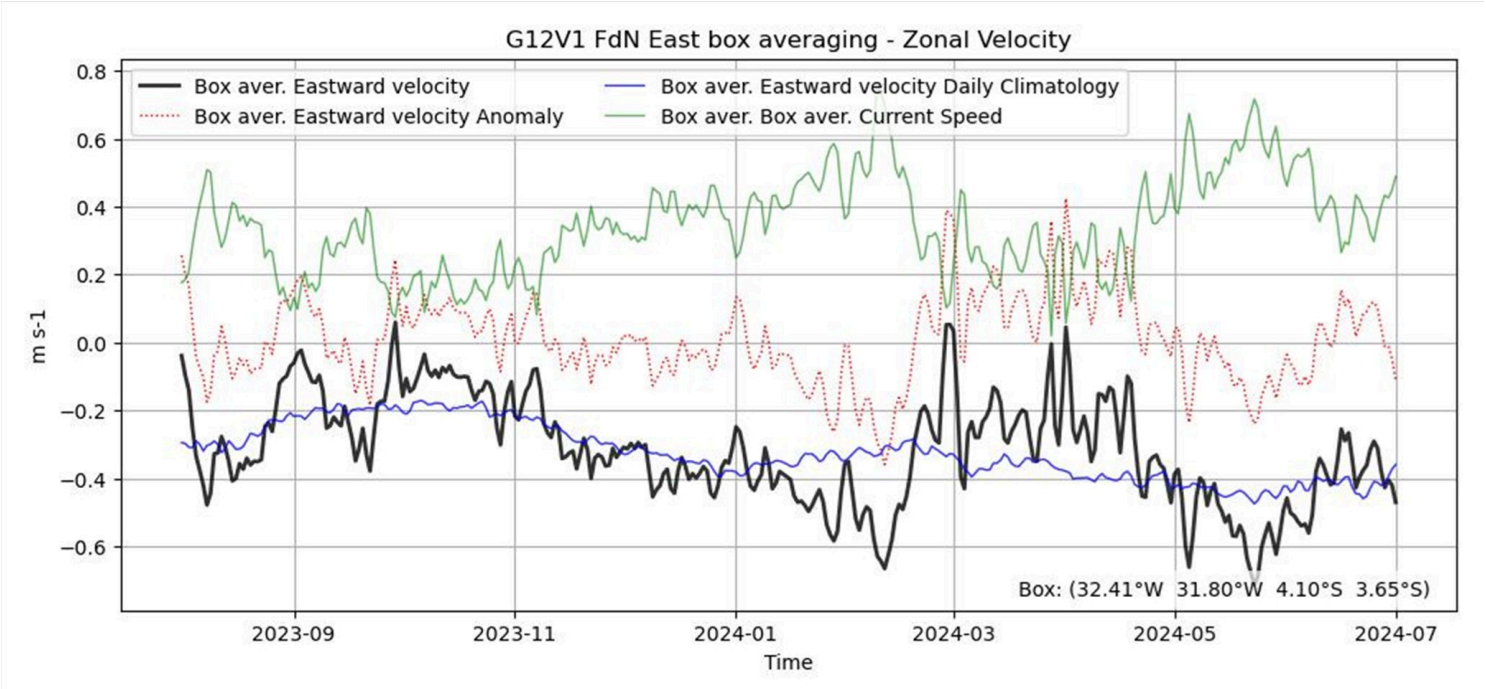


Figure 10

Time series of daily box averaged G12V1 zonal current east of FN (black) over the same period as the monthly eddy occurrence (Fig. 9), together with the daily climatology (blue) and the corresponding anomalies (red, dotted). The box averaged current speed (modulus of zonal and meridional component) is plotted in green

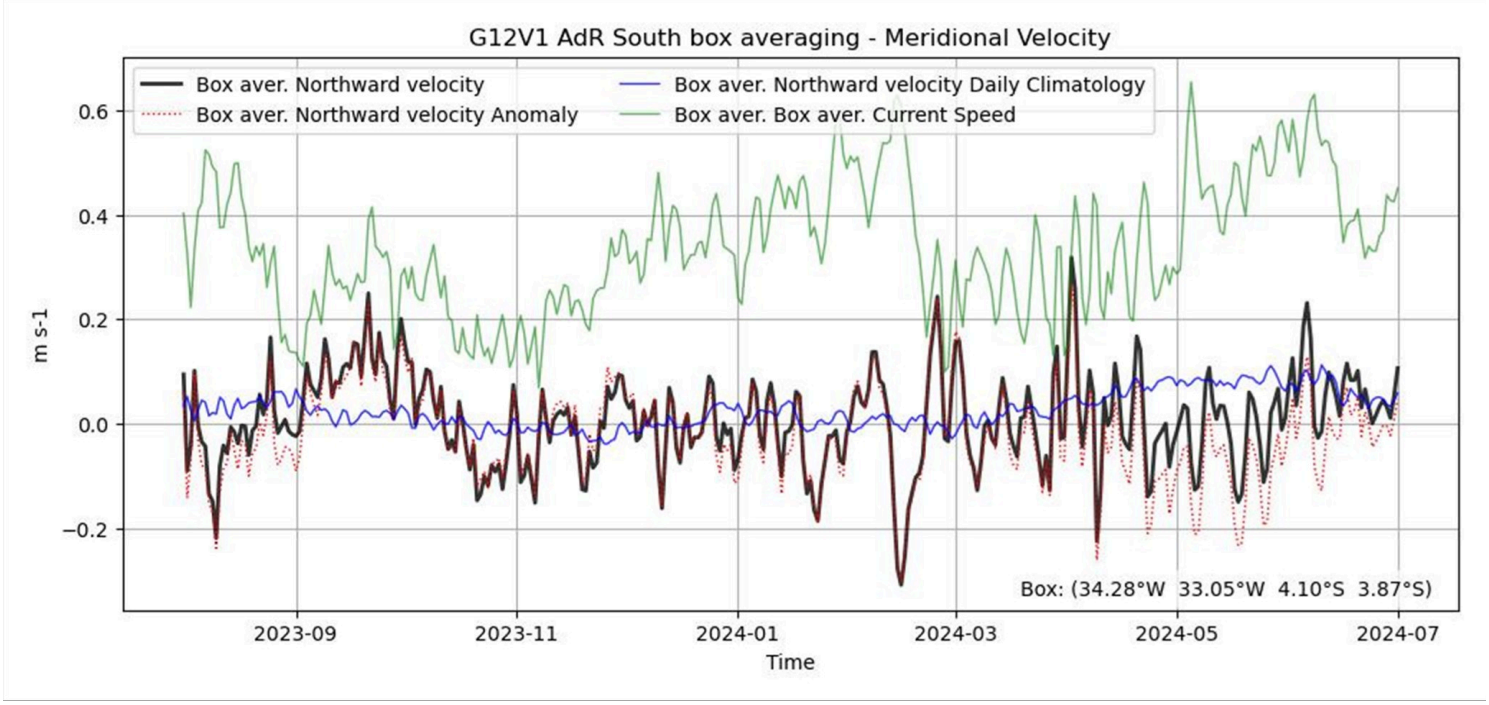


Figure 11

Time series of daily box averaged G12V1 meridional current south of AR (black) over the same period as the monthly eddy occurrence (Fig. 9), together with the daily climatology (blue) and the corresponding anomalies (red, dotted). The box averaged current speed (modulus of zonal and meridional component) is plotted in green

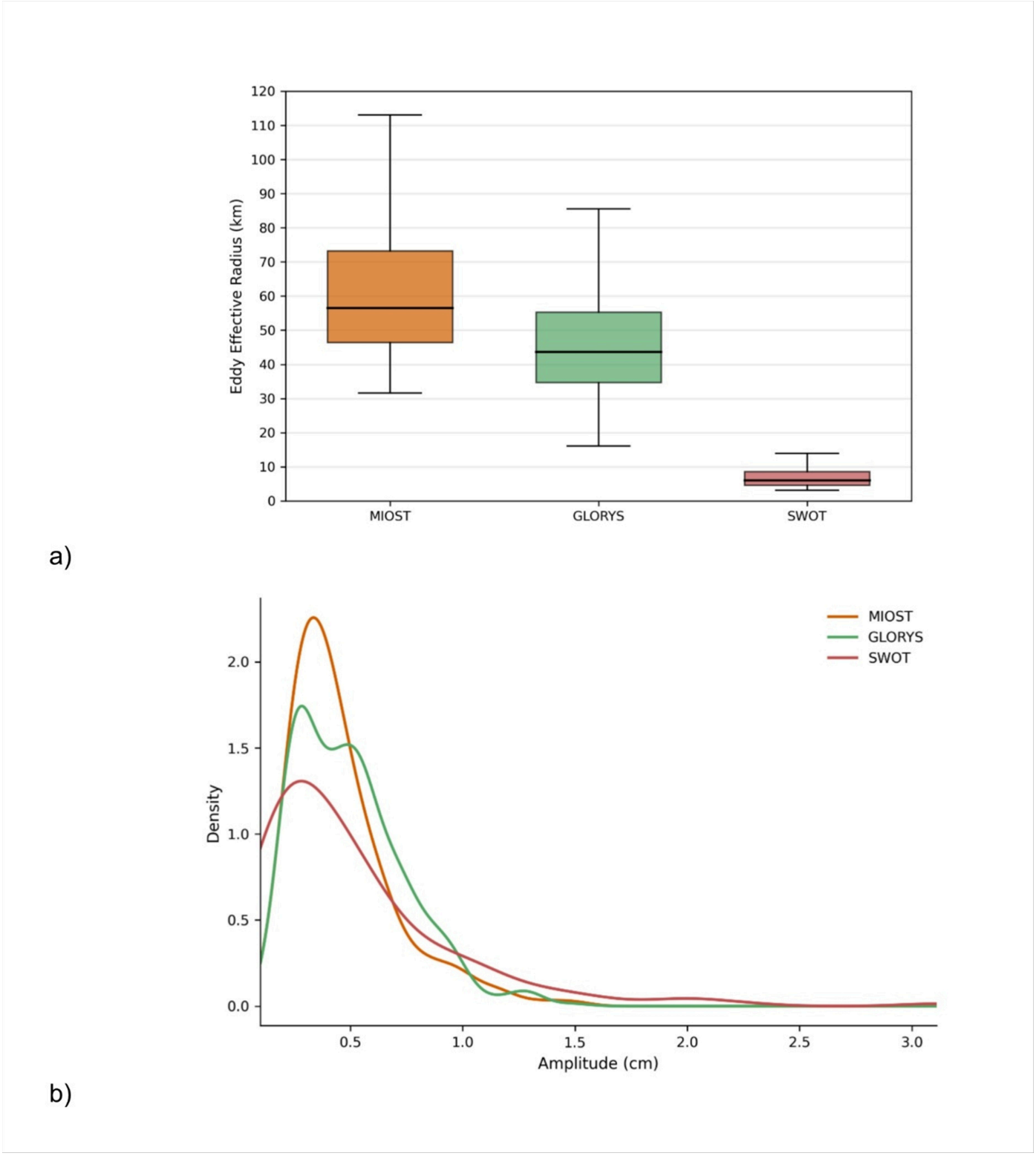


Figure 12

Comparison of eddy properties across datasets MIOST (orange), G12V1 (green) and SWOT (red). (a) Eddy effective radius (km) shown as boxplots. (b) Eddy amplitude (cm) distributions represented by kernel density estimates (KDE) for each dataset.